

ADAPTIVE PROBABILITY FLOW RESIDUAL MINIMIZATION FOR HIGH-DIMENSIONAL FOKKER-PLANCK EQUATIONS

XIAOLONG WU * AND QIFENG LIAO[†]

Abstract. Solving high-dimensional Fokker-Planck (FP) equations is a challenge in computational physics and stochastic dynamics, due to the curse of dimensionality (CoD) and the bottleneck of evaluating second-order diffusion terms. Existing deep learning approaches, such as Physics-Informed Neural Networks, face computational challenges as dimensionality increases, driven by the $O(d^2)$ complexity of automatic differentiation for second-order derivatives. While recent probability flow approaches bypass this by learning score functions or matching velocity fields, they often involve serial operations or depend on sampling efficiency in complex distributions. To address these issues, we propose the Adaptive Probability Flow Residual Minimization (A-PFRM) method. We reformulate the second-order FP equation into an equivalent first-order deterministic Probability Flow ODE (PF-ODE) constraint, which avoids explicit Hessian computation. Unlike score matching or velocity matching, A-PFRM solves this problem by minimizing the residual of the continuity equation induced by the PF-ODE. We leverage Continuous Normalizing Flows combined with the Hutchinson Trace Estimator to reduce the training complexity to linear scale $O(d)$, achieving an effective $O(1)$ wall-clock time on GPUs. To address data sparsity in high dimensions, we apply a generative adaptive sampling strategy and theoretically prove that dynamically aligning collocation points with the evolving probability mass is a necessary condition to bound the approximation error. Experiments on diverse benchmarks—ranging from anisotropic Ornstein-Uhlenbeck (OU) processes and high-dimensional Brownian motions with time-varying diffusion terms, to Geometric OU processes featuring non-Gaussian solutions—demonstrate that A-PFRM effectively mitigates the CoD, maintaining high accuracy and constant temporal cost for problems up to 100 dimensions.

Key words. Fokker-Planck equations; High-dimensional PDEs; Continuous normalizing flows; Hutchinson trace estimator; Adaptive sampling.

AMS subject classifications. 35Q84, 65M75, 68T07

1. Introduction. Stochastic dynamical systems play a pivotal role in modeling complex phenomena across a wide range of scientific and engineering disciplines, including molecular dynamics simulations [4], chemical reaction networks [18], biological systems modeling [23], and quantitative finance [32]. Quantifying the uncertainty in these systems typically involves characterizing the time evolution of the probability density function (PDF) of the state variables. This evolution is governed by the Fokker-Planck (FP) equation (also known as the Kolmogorov forward equation), a second-order partial differential equation (PDE) that describes the conservation of probability mass under the influence of drift and diffusion [40, 44].

While the theoretical foundations of the FP equation are well-established, obtaining numerical solutions for high-dimensional systems remains a persistent computational challenge. Traditional grid-based numerical methods, such as finite difference [42] and finite element methods [13], have been the workhorses for solving low-dimensional PDEs. However, these methods are constrained by the Curse of Dimensionality (CoD), as the computational cost of grid generation and linear algebra operations grows exponentially with the dimension of the system [9, 41]. To alleviate this issue, Monte Carlo (MC) simulation [5] is often employed as a mesh-free alternative. Although MC methods are theoretically insensitive to dimensionality, they exhibit a slow convergence rate proportional to $N^{-1/2}$. Furthermore, MC methods are often unsuitable for providing accurate point-wise estimates of the PDF in high-dimensional spaces. As dimensionality increases, the probability mass concentrates in specific regions (manifolds), causing PDF values to decay exponentially and fall below machine precision,

*School of Information Science and Technology, ShanghaiTech University, Shanghai 201210, China (wuxl2024@shanghai.tech.edu.cn).

[†]School of Information Science and Technology, ShanghaiTech University, Shanghai 201210, China (liaoqf@shanghaitech.edu.cn).

resulting in numerical underflow [36].

In recent years, deep learning has emerged as a promising paradigm for solving high-dimensional PDEs, leveraging the universal approximation capability of deep neural networks [19]. Widely used methods such as Physics-Informed Neural Networks (PINNs) [38], the Deep Galerkin Method [43], and the Deep Ritz Method [12] formulate the PDE problem as an optimization task, minimizing the residual of the governing equation at randomly sampled collocation points. To further address the CoD and enhance training efficiency, recent studies have introduced advanced numerical structures and sampling strategies. For instance, functional hierarchical tensors have been utilized to solve high-dimensional FP equations effectively [49], while a hybrid sampling scheme was developed in [25] to improve the resolution of complex probability landscapes. Furthermore, a mesh-free solver incorporating MC reference data was proposed in [53] to handle unbounded domains, and a framework combining PINNs with Kullback-Leibler divergence was introduced in [8] to solve inverse stochastic problems from discrete particle observations. Among these, generative models, particularly Normalizing Flows (NFs) [27, 36], have shown great potential due to their ability to provide exact likelihood evaluations. Specifically, an adaptive deep density approximation strategy based on KRnet was introduced in [47] to efficiently solve steady-state FP equations. In addition, the Weak Generative Sampler [6] was proposed to efficiently sample the invariant distributions of high-dimensional SDEs via a weak formulation strategy. For time-evolving systems, temporal NFs have been developed to directly model the time-evolution of probability densities for standard FP equations [15]. Subsequently, the temporal KRnet (tKRnet) was proposed [21], incorporating a time-dependent flow structure and adaptive sampling to solve the continuity equation associated with stochastic dynamical systems driven by uncertain parameters. More recently, the variational conditional NF [54] was introduced to address Mean Field Control problems and the associated FP equations. With score-based generative models [45], Score-PINNs [24] were proposed to solve the FP equation by learning the score function, typically minimizing the residual of the score-PDE.

Beyond these approaches, a new paradigm has recently emerged that fundamentally reformulates the FP equation into an equivalent first-order deterministic Probability Flow ordinary differential equation (PF-ODE), thereby mathematically avoiding the explicit calculation of the computationally expensive Hessian matrix. Pioneering works [3, 30] have successfully applied this framework to solve mass-conserving PDEs. Representative strategies include iteratively updating the velocity field to satisfy consistency conditions derived from the continuity equation [30], or learning the probability flow via score-matching objectives [3]. However, extending the PF-ODE framework to high-dimensional regimes requires addressing specific computational characteristics. For instance, optimization frameworks relying on ODE adjoint sensitivity analysis typically involve sequential integration backward in time, which introduces a temporal dependency in the computational graph. Alternatively, approaches leveraging samples directly from the underlying SDE are inherently bound by the exploration efficiency of the stochastic dynamics, typically following standard MC convergence rates ($N^{-1/2}$).

To address these challenges and fully realize the scalability of the probability flow framework, we propose a novel framework termed Adaptive Probability Flow Residual Minimization (A-PFMR). The main idea of our approach is to reformulate the second-order FP equation into an equivalent first-order PF-ODE constraint. Unlike standard velocity matching approaches that often treat the target velocity as a fixed reference, A-PFMR solves the problem by directly minimizing the residual of the PF-ODE continuity equation. This formulation avoids the $O(d^2)$ Hessian bottleneck inherent in standard PINNs while retaining the optimization robustness of full gradient flow. To achieve scalability within this framework,

through integrating Continuous Normalizing Flows (CNF) [7] with the Hutchinson Trace Estimator (HTE) [20], the exact trace calculations are transformed into parallelizable stochastic vector-Jacobian products. Furthermore, to tackle the data sparsity in high-dimensional spaces, the generative adaptive sampling strategy [47] is applied to dynamically allocate collocation points to high-probability regions generated by the flow itself. The collocation points here are for the spatial variable, while stochastic collocation for parameters in PDEs with random inputs is discussed in detail in [51, 52, 1, 16, 33, 34, 28].

In summary, the main contributions of this work are threefold. First, regarding scalability, we demonstrate that by converting the serial complexity of the Jacobian trace into parallelizable operations, A-PFRM achieves effectively $O(1)$ wall-clock training time on GPUs, enabling efficient scaling to 100 dimensions with constant temporal cost. Second, we provide a theoretical analysis revealing that our generative adaptive sampling is more than a heuristic, serving as a necessary condition to bound the Wasserstein distance error, establishing a rigorous consistency between theory and practice. Third, we demonstrate the method's robustness on complex benchmarks, including high-dimensional systems with time-varying diffusion and non-Gaussian heavy-tailed solutions. The rest of this paper is organized as follows. Section 2 outlines the problem setup. Section 3 reviews mathematical preliminaries. Section 4 details the A-PFRM methodology, including the scalable implementation, adaptive sampling strategy, and theoretical convergence analysis. Section 5 presents numerical experiments on high-dimensional benchmarks, followed by conclusions in Section 6.

2. Problem Setup. Consider the state X_t modeled by the following SDE:

$$(2.1) \quad dX_t = \mathbf{f}(X_t, t)dt + \mathbf{G}(X_t, t)dW_t,$$

where $X_t \in \mathbb{R}^d, t \in [0, T], T$ is the terminal time, $W_t \in \mathbb{R}^d$ is a Brownian motion, the drift function $\mathbf{f}(X_t, t) : \mathbb{R}^d \times \mathbb{R} \rightarrow \mathbb{R}^d$ and the diffusion function $\mathbf{G}(X_t, t) : \mathbb{R}^d \times \mathbb{R} \rightarrow \mathbb{R}^{d \times d}$ are known in the SDE. The FP equation [35], which describes the evolution of the PDF $p_t(X_t) : X_t \sim p_t(X_t)$ modeled by the SDE Eq.(2.1), is

$$(2.2) \quad \frac{\partial p_t(\mathbf{x})}{\partial t} = \mathcal{F}[p_t(\mathbf{x})] = -\nabla \cdot [p_t(\mathbf{x})\mathbf{f}(\mathbf{x}, t)] + \nabla \cdot \left\{ \nabla \cdot [p_t(\mathbf{x})\mathbf{D}(\mathbf{x}, t)] \right\},$$

$$(2.3) \quad \int_{\mathbb{R}^d} p_t(\mathbf{x})d\mathbf{x} = 1, \quad p_t(\mathbf{x}) \geq 0, \quad \forall t \in [0, T],$$

$$(2.4) \quad p_0(\mathbf{x}) = p_{\text{IC}}(\mathbf{x}),$$

where $\mathbf{x} \in \mathbb{R}^d$ denotes a random vector, \mathcal{F} denotes the partial differential operator, $\mathbf{D}(\mathbf{x}, t) = \frac{1}{2}\mathbf{G}(\mathbf{x}, t)\mathbf{G}(\mathbf{x}, t)^T$ is a diffusion matrix, $p_{\text{IC}}(\mathbf{x})$ is the initial PDF of \mathbf{x} , and the main equation Eq.(2.2) can be further expressed as:

$$(2.5) \quad \frac{\partial p_t(\mathbf{x})}{\partial t} = -\sum_{i=1}^d \frac{\partial}{\partial x_i} [f_i(\mathbf{x}, t)p_t(\mathbf{x})] + \frac{1}{2} \sum_{i,j=1}^d \frac{\partial^2}{\partial x_i \partial x_j} \left[\sum_{k=1}^d G_{ik}(\mathbf{x}, t)G_{kj}(\mathbf{x}, t)p_t(\mathbf{x}) \right].$$

In this work, we focus on the forward problem of SDE Eq.(2.1), i.e., given the initial distribution $p_0(X_0) = p_{\text{IC}}(X_0)$ at $t = 0$ and the SDE coefficients, how does the distribution of X_t evolve over time $t \in [0, T]$?

Although the operator \mathcal{F} is linear, there are several difficulties for solving FP equation. First, when we adopt traditional grid-based approaches, such as the finite element method, it is challenging to strictly enforce the normalization and non-negativity constraints of $p_t(\mathbf{x})$ Eq.(2.3), as well as the derived boundary condition:

$$(2.6) \quad p(\mathbf{x}) \rightarrow 0 \quad \text{as} \quad \|\mathbf{x}\|_2 \rightarrow \infty.$$

Since the support of $p(\boldsymbol{x})$ is \mathbb{R}^d while the practical computation domain is finite, a truncation error inevitably arises at the boundaries. A projection step is also needed to preserve the non-negativity of $p(\boldsymbol{x})$ for the box constraint. Second, the state variable $\boldsymbol{x} \in \mathbb{R}^d$ is often of high dimensions. Traditional grid-based numerical methods are constrained by the CoD, whose computational costs typically increase exponentially with dimension d . While the deeply based methods are actively developed to overcome the CoD, optimizing the objective function in high-dimensional spaces can still be challenging. A main difficulty is the value of the PDF itself. As the dimension d increases, the value of $p(\boldsymbol{x})$ rapidly approaches zero, leading to significant numerical underflow and round-off errors [24]. Third, when the target density $p(\boldsymbol{x})$ is multimodal, a very fine mesh or a highly expressive model is required to capture its complex structure. This is particularly challenging when d is large. To address these issues, this work is to propose a first-order residual based on the equivalence transformation between SDEs and deterministic PF-ODEs, combined with a flow-based generative adaptive sampling strategy. The flow-based generative model naturally satisfies the constraints of the probability distribution $p(\boldsymbol{x})$; reducing the equation order to a first-order PF-ODE effectively mitigates the CoD; the adaptive sampling strategy generates an efficient set of sampling points to capture complex structures.

3. Preliminary.

3.1. Density Approximation via Continuous Normalizing Flows. A fundamental task in solving the FP equation is constructing a density estimator that strictly satisfies the normalization constraint and boundary conditions. NFs [39] address this by learning a diffeomorphism $\boldsymbol{z}_1 = \boldsymbol{f}(\boldsymbol{z}_0)$ that pushes a simple reference measure p_0 (e.g., a standard Gaussian) to the target measure p_1 . The density evolution is governed by the change-of-variables formula involving the Jacobian determinant $\det(\nabla \boldsymbol{f})$:

$$(3.1) \quad \log p_1(\boldsymbol{z}_1) = \log p_0(\boldsymbol{z}_0) - \log \left| \det \left(\frac{\partial \boldsymbol{f}}{\partial \boldsymbol{z}_0} \right) \right|.$$

However, computing this determinant typically incurs a cubic computational complexity $O(d^3)$, which forces standard NFs to adopt restricted architectures (e.g., triangular mappings [11]), thereby limiting their expressive power in approximating complex transport maps.

To overcome this bottleneck, CNFs [7] parameterize the transport map as the flow of an ODE. Instead of discrete layers, CNFs define the continuous dynamics of a state variable $\boldsymbol{z}(t)$ via a learnable velocity field $\boldsymbol{u}_\theta(\boldsymbol{z}, t)$:

$$(3.2) \quad \frac{d\boldsymbol{z}(t)}{dt} = \boldsymbol{u}_\theta(\boldsymbol{z}(t), t), \quad \boldsymbol{z}(0) \sim p_0.$$

From the perspective of fluid dynamics, the evolution of the log-probability density $\log \mu_t(\boldsymbol{z}(t))$ along the characteristic lines (trajectories) satisfies the instantaneous change of variables formula:

$$(3.3) \quad \frac{\partial \log p(\boldsymbol{z}(t))}{\partial t} = -\nabla \cdot \boldsymbol{u}_\theta(\boldsymbol{z}(t), t) = -\text{tr} \left(\frac{\partial \boldsymbol{u}_\theta}{\partial \boldsymbol{z}} \right).$$

This continuous formulation simplifies the geometric cost from calculating a determinant to calculating the trace of the Jacobian matrix $\nabla \boldsymbol{u}_\theta$.

While the trace operation $O(d)$ is theoretically simpler than the determinant $O(d^3)$, explicitly forming the Jacobian matrix via automatic differentiation [2] still requires d backward passes, leading to $O(d^2)$ complexity for the full trace. To achieve scalability for high-dimensional problems, we employ the HTE [20], a MC method that approximates the trace

via stochastic projection:

$$(3.4) \quad \text{tr} \left(\frac{\partial \mathbf{u}_\theta}{\partial \mathbf{z}} \right) = \mathbb{E}_{p_{\text{noise}}(\epsilon)} \left[\epsilon^T \frac{\partial \mathbf{u}_\theta}{\partial \mathbf{z}} \epsilon \right],$$

where $\epsilon \in \mathbb{R}^d$ is a noise vector drawn from a noise distribution with zero mean and unit covariance (e.g., Rademacher distribution). Crucially, the term $\epsilon^T \frac{\partial \mathbf{u}_\theta}{\partial \mathbf{z}}$ can be computed efficiently as a vector-Jacobian product using reverse-mode automatic differentiation [2]. This allows the divergence term to be evaluated in effectively $O(1)$ wall-clock time on parallel architectures, avoiding the explicit instantiation of the Jacobian matrix and breaking the memory bottleneck associated with high-dimensional grids.

3.2. Probability Flow Formulation of Stochastic Dynamics. Our method is grounded in the theoretical equivalence between SDEs and deterministic PF-ODEs, a new concept from recent advances in Score-Based Generative Models [45]. It has been proved that there exists a deterministic process satisfying an ODE, whose trajectories share the exact same time-dependent marginal densities $\{p_t(\mathbf{x})\}_{t=0}^T$ as the SDE of the form shown in Eq.(2.1). This equivalent deterministic process, termed the PF-ODE, is given by:

$$(3.5) \quad dX_t = \left[\mathbf{f}(X_t, t) - \nabla \cdot \mathbf{D}(X_t, t) - \mathbf{D}(X_t, t) \nabla \log p_t(X_t) \right] dt,$$

where $\mathbf{D}(X_t, t) = \frac{1}{2} \mathbf{G}(X_t, t) \mathbf{G}(X_t, t)^T$ is the diffusion matrix. Eq.(3.5) implies that the diffusive behavior of the stochastic system—macroscopically manifested as the second-order diffusion term in the FP equation—can be fully captured by a deterministic convection guided by the score function $\nabla \log p_t$.

This theoretical result serves as the foundation of our A-PFRM method. Instead of simulating stochastic paths (which are limited by slow $N^{-1/2}$ convergence) or solving the second-order PDE directly (which requires computationally intensive Hessian evaluation), we aim to learn the velocity field $\mathbf{v}_t(\mathbf{x})$ of this equivalent ODE. While recent approaches like Flow Matching [31] propose regressing this velocity field from data samples using conditional paths, our goal is to determine the velocity field by minimizing the residual of the probability flow continuity equation derived from the FP operator, without requiring ground-truth samples from the solution.

4. Adaptive Probability Flow Residual Minimization.

4.1. Determining the Probability Flow Dynamics. To solve the high-dimensional FP equation efficiently, we adopt the probability flow formulation established in Section 3.2. Instead of solving the second-order PDE directly, our goal is to construct a CNF model $\mathbf{u}_\theta(\mathbf{x}, t)$ that satisfies the governing equation of the deterministic PF-ODE.

Given the drift function $\mathbf{f}(\mathbf{x}, t)$ and the diffusion function $\mathbf{G}(\mathbf{x}, t)$ from the original SDE Eq.(2.1), the theoretical target velocity field $\mathbf{v}_t(\mathbf{x})$ required to transport the probability mass consistently with the FP equation is derived as:

$$(4.1) \quad \mathbf{v}_t(\mathbf{x}) \triangleq \mathbf{f}(\mathbf{x}, t) - \nabla \cdot \mathbf{D}(\mathbf{x}, t) - \mathbf{D}(\mathbf{x}, t) \nabla \log p_t(\mathbf{x}),$$

where $\mathbf{D}(\mathbf{x}, t) = \frac{1}{2} \mathbf{G}(\mathbf{x}, t) \mathbf{G}(\mathbf{x}, t)^T$ is the diffusion matrix and $\nabla \log p_t(\mathbf{x})$ is the score function of the instantaneous density.

This formulation effectively converts the second-order FP equation into a first-order continuity equation constraint:

$$(4.2) \quad \frac{\partial p_t(\mathbf{x})}{\partial t} + \nabla \cdot [p_t(\mathbf{x}) \mathbf{v}_t(\mathbf{x})] = 0.$$

Equivalently, this velocity field defines the trajectories of the deterministic PF-ODE:

$$(4.3) \quad \frac{dX_t}{dt} = \mathbf{v}_t(X_t).$$

In the A-PFRM framework, if a velocity field \mathbf{u}_θ satisfies Eq.(4.1) for the density \hat{p}_t it generates, the resulting flow \hat{X}_t (starting from $X_0 \sim p_0$) will theoretically match the exact solution of the original FP equation (detailed in Proposition 4.1).

4.2. Score Estimation via Scalable Continuous Normalizing Flow. This subsection introduces the core mechanism for estimating the instantaneous probability density and its score. We employ a Neural ODE [7] to parameterize the velocity field, and leverage CNFs to track the density evolution.

We approximate the unknown velocity field using a neural network $\mathbf{u}_\theta(\mathbf{x}, t)$ with parameters θ . The resulting generative dynamics are defined by:

$$(4.4) \quad \frac{d\hat{X}_t}{dt} = \mathbf{u}_\theta(\hat{X}_t, t).$$

To evaluate the governing equation Eq.(4.1), we must compute the score $\nabla \log \hat{p}_t(\mathbf{x}; \theta)$ of the density generated by this network. According to the instantaneous change of variables formula, the log-density evolves as:

$$(4.5) \quad \log \hat{p}_t(\mathbf{x}_t; \theta) = \log p_0(\mathbf{x}_0) - \int_0^t \nabla \cdot \mathbf{u}_\theta(\mathbf{x}_s, s) ds, \quad \forall \mathbf{x}_t \in \mathbb{R}^d, t \in (0, T]$$

where \mathbf{x}_s for $s \in [0, t]$ is the trajectory solving Eq.(4.4) passing through \mathbf{x}_t at time t and \mathbf{x}_s can be obtained through

$$(4.6) \quad \mathbf{x}_t - \mathbf{x}_s = \int_s^t \mathbf{u}_\theta(\mathbf{x}_\xi, \xi) d\xi, \quad s \in [0, t),$$

specifically, \mathbf{x}_0 denotes the state at time $s = 0$ along this trajectory.

Directly computing the divergence $\nabla \cdot \mathbf{u}_\theta$ in Eq.(4.5) via automatic differentiation [2] requires d backward passes, scaling as $O(d^2)$ or serial $O(d)$. To ensure the scalability proposed in our A-PFRM framework, we replace the exact divergence with the HTE during training:

$$(4.7) \quad \nabla \cdot \mathbf{u}_\theta(\mathbf{x}, t) = \text{tr} \left(\frac{\partial \mathbf{u}_\theta}{\partial \mathbf{x}} \right) \approx \epsilon^T \frac{\partial \mathbf{u}_\theta}{\partial \mathbf{x}} \epsilon, \quad \epsilon \sim p_{\text{noise}}(\epsilon),$$

where ϵ is a noise vector (e.g., Rademacher distribution). This allows us to evaluate the dynamics in effectively $O(1)$ wall-clock time on parallel hardware using vector-Jacobian products, decoupling the computation time from the dimensionality d .

Computing \mathbf{x}_0 and the integral requires solving the Neural ODE. This is efficiently done by constructing an augmented ODE system [7]. It augments the state \mathbf{x} with an additional variable, I , then, the augmented system is:

$$(4.8) \quad \frac{d}{ds} \begin{pmatrix} \mathbf{x}_s \\ I_s \end{pmatrix} = \begin{pmatrix} \mathbf{u}_\theta(\mathbf{x}_s, s) \\ -\nabla \cdot \mathbf{u}_\theta(\mathbf{x}_s, s) \end{pmatrix}.$$

The procedure to compute $\log \hat{p}_t(\mathbf{x}_t; \theta)$ for a given (\mathbf{x}_t, t) using HTE technique is thus:

- Initialize the augmented state at time t as $[\mathbf{x}_t, I_t]^T$, $I_t = 0$.
- Solve the augmented ODE Eq.(4.8) backwards in time from t to 0 using a numerical ODE solver (e.g., 4-th order Runge-Kutta method), utilizing the HTE for the divergence term at each function evaluation.

- Obtain the initial state $[\mathbf{x}_0, I_0]^T$, where

$$(4.9) \quad I_0 = I_0 - I_t = \int_t^0 \left(-\nabla_{\text{HTE}} \cdot \mathbf{u}_\theta(\mathbf{x}_s, s) \right) ds = \int_0^t \nabla_{\text{HTE}} \cdot \mathbf{u}_\theta(\mathbf{x}_s, s) ds.$$

- Compute the final log-density using the initial density p_0 :

$$(4.10) \quad \log \hat{p}_t(\mathbf{x}_t; \theta) = \log p_0(\mathbf{x}_0) - \int_0^t \nabla_{\text{HTE}} \cdot \mathbf{u}_\theta(\mathbf{x}_s, s) ds = \log p_0(\mathbf{x}_0) - I_0.$$

Finally, to obtain the score $\nabla_{\mathbf{x}} \log \hat{p}_t(\mathbf{x}; \theta)$ required for the loss function, we perform automatic differentiation through the ODE solver. Thanks to the HTE, the spatial complexity of this backward pass remains efficient even in high dimensions.

4.3. The Probability Flow Residual Loss (First-Order Formulation). Having established the PF-ODE framework and the scalable score estimation, we now construct the optimization objective. Unlike velocity matching approaches that treat the target velocity as a fixed reference, we formulate the training as minimizing the residual of the probability flow equation.

The condition for \mathbf{u}_θ to be a valid solution is that it must strictly satisfy the PF-ODE relation derived in Eq.(4.1). We define the probability flow residual $\mathcal{R}(\mathbf{x}, t; \theta)$ as the difference between the network’s output velocity and the physical velocity dictated by its generated density \hat{p}_t :

$$(4.11) \quad \mathcal{R}(\mathbf{x}, t; \theta) \triangleq \mathbf{u}_\theta(\mathbf{x}, t) - \left[\mathbf{f}(\mathbf{x}, t) - \nabla \cdot \mathbf{D}(\mathbf{x}, t) - \mathbf{D}(\mathbf{x}, t) \nabla_{\mathbf{x}} \log \hat{p}_t(\mathbf{x}; \theta) \right].$$

The loss function is defined as the expected squared norm of this residual:

$$(4.12) \quad \mathcal{L}(\theta) = \mathbb{E}_{(\mathbf{x}, t) \sim \mathcal{D}} \left[\|\mathcal{R}(\mathbf{x}, t; \theta)\|_2^2 \right].$$

Standard PINNs for the FP equation minimize the residual of the second-order PDE:

$$(4.13) \quad \mathcal{L}_{\text{Standard PINNs}} [p] = \left\| \partial_t p + \nabla \cdot (\mathbf{f} p) - \nabla \cdot (\nabla \cdot (\mathbf{D} p)) \right\|^2$$

Computing the diffusion term in standard PINNs requires calculating the Hessian trace, which scales as $O(d^2)$. In contrast, A-PFRM transforms this second-order PDE constraint into a first-order ODE constraint Eq.(4.12). The highest-order derivative in our loss is the score $\nabla \log p$, which is a first-order spatial derivative. By combining this formulation with the HTE for density computation, we avoid explicit Hessian calculations.

Crucially, we maintain the full computational graph of $\mathcal{R}(\mathbf{x}, t; \theta)$ during optimization. The gradient $\nabla_\theta \mathcal{L}$ propagates through both the explicit velocity term \mathbf{u}_θ and the implicit score term $\nabla \log \hat{p}_t$ (which depends on θ via the CNF integration path). This allows the optimizer to adjust parameters θ by considering how changes in the vector field simultaneously affect the particle velocity and the resulting probability density evolution, ensuring dynamic consistency for complex, non-Gaussian distributions.

4.4. Adaptive Sampling-based Training Procedure. This subsection outlines the practical algorithm used to train the neural velocity field $\mathbf{u}_\theta(\mathbf{x}, t)$ by minimizing the probability flow residual loss function $\mathcal{L}(\theta)$ defined in Eq.(4.12). A key challenge in minimizing the residual is the choice of the sampling distribution \mathcal{D} for the spatio-temporal points (\mathbf{x}, t) used to approximate the expectation via MC methods during SGD (e.g., Adam [26]). While simple choices like uniform sampling over a bounded domain Ω are possible, they can become

inefficient, especially when the solution density $p_t(\mathbf{x}, t)$ is concentrated in specific regions, a situation exacerbated by the CoD [48]. Uniform collocation points land in regions where both the probability mass and the gradients are vanishingly small, providing zero informative gradients for optimization [48, 17].

To address this, we adopt a generative adaptive sampling strategy, which has been proven effective in improving the training efficiency of deep density estimators for steady-state FP equations [47]. The main idea is to leverage the generative nature of the learned CNF $\mathbf{u}_\theta(\mathbf{x}, t)$ itself to produce collocation points that track the evolving probability mass. By evaluating the residual $\mathcal{R}(\mathbf{x}, t; \theta)$ on samples generated by the current model, we ensure that the physical constraints are enforced exactly where the probability mass is concentrated—on the support of the distribution. The adaptive sampling-based loss takes the form:

$$(4.14) \quad \mathcal{L}_{\text{Adapt}}(\theta) = \mathbb{E}_{t \sim U[0, T]} [\mathcal{L}_{\text{Adapt}}(\theta, t)] = \mathbb{E}_{t \sim U[0, T], \mathbf{x} \sim \hat{p}_t} [\|\mathcal{R}(\mathbf{x}, t; \theta)\|_2^2].$$

The complete procedure is detailed in Algorithm 1.

The training follows a three-phase curriculum (Warm-up, Ramp-up, Stable Adaptive) to ensure stability.

- **Warm-up Phase:** ($\alpha_{\text{current}} = 0.0$) Purely uniform sampling allows the network to learn the global drift and diffusion fields without being biased by the initially incorrect flow.
- **Ramp-up Phase:** The ratio of adaptive samples is linearly increased. This smooth transition prevents "mode collapse" where the flow might converge to a local trap if the adaptive feedback loop is closed too early.
- **Stable Adaptive Phase:** ($\alpha_{\text{current}} = \alpha_{\text{adapt}}$) The training focuses on the high-probability regions (exploitation) while retaining a component of uniform samples (exploration) to ensure global boundary conditions are met.

Inside each epoch, we iterate through a fixed time schedule $\{t_s\}_{s=1}^{N_T}$ to reduce variance. For each time step, we construct a hybrid batch \mathcal{B}_x containing both adaptive samples (generated by solving the CNF augmented ODE forward from p_0) and uniform samples. The gradient update is then performed by minimizing the residual on this batch.

4.5. Convergence analysis and Error estimation. In this subsection, we provide a theoretical analysis of the proposed A-PFRM method. Specifically, we establish the validity of the residual minimization framework, demonstrating that if the probability flow residual converges to zero, the generated density path rigorously satisfies the original FP equation. Furthermore, we derive an upper bound for the growth of the 2-Wasserstein error, explicitly linking it to the training residual and the sampling strategy.

4.5.1. Validity of the Residual Minimization. Let $\mathbf{u}_\theta(\mathbf{x}, t)$ be the neural velocity field and $\hat{p}_t(\mathbf{x}; \theta)$ be the density generated by \mathbf{u}_θ via the CNF, starting from the initial condition p_0 . Recall from Section 4.3 that our training objective is to minimize the expected squared norm of the probability flow residual $\mathcal{R}(\mathbf{x}, t; \theta)$:

$$(4.15) \quad \mathcal{L}(\theta) = \mathbb{E}_{(\mathbf{x}, t) \sim \mathcal{D}} [\|\mathcal{R}(\mathbf{x}, t; \theta)\|_2^2],$$

where the residual is defined as the mismatch between the neural velocity and the physical velocity dictated by the generated density:

$$(4.16) \quad \mathcal{R}(\mathbf{x}, t; \theta) \triangleq \mathbf{u}_\theta(\mathbf{x}, t) - [\mathbf{f}(\mathbf{x}, t) - \nabla \cdot \mathbf{D}(\mathbf{x}, t) - \mathbf{D}(\mathbf{x}, t) \nabla \log \hat{p}_t(\mathbf{x}; \theta)].$$

PROPOSITION 4.1 (Validity of the Probability Flow Residual). *Assuming the neural network \mathbf{u}_θ has sufficient capacity (Universal Approximation Property [10, 29]), if the residual loss*

Algorithm 1 Adaptive Probability Flow Residual Minimization (A-PFRM)

Require: Initial neural network \mathbf{u}_θ with parameters Θ_0 , initial condition $p_0(\mathbf{x}) = p_{\text{IC}}(\mathbf{x})$, drift function $\mathbf{f}_t(\mathbf{x})$, diffusion function $D_t(\mathbf{x})$, total number of training epochs N_{epochs} , learning rate η , batch size N_x , time schedule $\{t_s\}_{s=1}^{N_T} \subset (0, T]$, domain of interest Ω , number of warm-up epochs N_{warmup} , number of ramp-up epochs N_{rampup} , final adaptive sampling ratio $\alpha_{\text{adapt}} \in [0, 1]$.

- 1: Initialize parameters $\Theta_1^{(1)} \leftarrow \Theta_0$.
- 2: **for** $j = 1$ **to** N_{epochs} **do**
- 3: Update adaptive ratio α_{current} based on current epoch (Warm-up / Ramp-up / Stable).
- 4: **for** each time step t_s in $\{t_s\}_{s=1}^{N_T}$ **do**
- 5: **Step 1: Batch Generation**
- 6: **if** $\alpha_{\text{current}} > 0$ **then**
- 7: Generate adaptive samples $\{\mathbf{x}_{\text{adapt}}^{(i)}\}$ by solving $\frac{d\mathbf{x}}{d\tau} = \mathbf{u}_{\Theta^{(j)}}(\mathbf{x}, \tau)$ from 0 to t_s .
- 8: **end if**
- 9: Generate uniform samples $\{\mathbf{x}_{\text{uniform}}^{(i)}\}$.
- 10: Combine to form batch $\mathcal{B}_x = \{\mathbf{x}_{\text{adapt}}^{(i)}\} \cup \{\mathbf{x}_{\text{uniform}}^{(i)}\}$.
- 11: **Step 2: Residual Minimization**
- 12: **for** each $\mathbf{x}_i \in \mathcal{B}_x$ **do**
- 13: Compute $\log \hat{p}_{t_s}(\mathbf{x}_i; \Theta_s^{(j)})$ via CNF (augmented ODE with HTE).
- 14: Compute score $\mathbf{s}_i = \nabla_{\mathbf{x}} \log \hat{p}_{t_s}(\mathbf{x}_i; \Theta_s^{(j)})$ via Autograd.
- 15: Evaluate PF-ODE Residual:

$$\mathcal{R}_i = \mathbf{u}_{\Theta^{(j)}}(\mathbf{x}_i, t_s) - \left[\mathbf{f}(\mathbf{x}_i, t_s) - \nabla \cdot D(\mathbf{x}_i, t_s) - D(\mathbf{x}_i, t_s) \mathbf{s}_i \right]$$
- 16: **end for**
- 17: Compute Loss $L_{\text{batch}} \leftarrow \frac{1}{N_x} \sum_{i=1}^{N_x} \|\mathcal{R}_i\|_2^2$.
- 18: Compute gradient $g \leftarrow \nabla_{\Theta} L_{\text{batch}}$ (maintaining full computational graph).
- 19: Update parameters: $\Theta_{s+1}^{(j)} \leftarrow \text{OptimizerStep}(\Theta_s^{(j)}, g, \eta)$.
- 20: **end for**
- 21: $\Theta_1^{(j+1)} \leftarrow \Theta_{N_T}^{(j)}$.
- 22: **end for**
- 23: **return** Neural network \mathbf{u}_θ with final trained parameters $\Theta_{N_T}^{N_{\text{epochs}}}$ and the learned density $\hat{p}_t(\mathbf{x}; \theta)$ can be obtained by \mathbf{u}_θ through CNF augmented ODE.

converges to zero, i.e., $\mathcal{L}(\theta^*) \rightarrow 0$ over the domain $\Omega \times [0, T]$, then the generated probability density function $\hat{p}_t(\mathbf{x}; \theta^*)$ is a solution to the Fokker-Planck equation Eq.(2.2). Furthermore, if the drift function $\mathbf{f}(\mathbf{x}, t)$ and diffusion function \mathbf{G} are Lipschitz-continuous with respect to \mathbf{x} , this solution is unique.

Proof. The time-evolution of the generated density \hat{p}_t is governed by the continuity equation of the neural vector field \mathbf{u}_{θ^*} :

$$(4.17) \quad \frac{\partial \hat{p}_t}{\partial t} + \nabla \cdot (\hat{p}_t \mathbf{u}_{\theta^*}) = 0.$$

If the loss $\mathcal{L}(\theta^*) \rightarrow 0$, it implies that the residual $\mathcal{R}(\mathbf{x}, t; \theta^*) = 0$ almost everywhere with respect to the measure \mathcal{D} . This leads to the condition:

$$(4.18) \quad \mathbf{u}_{\theta^*}(\mathbf{x}, t) = \mathbf{f}(\mathbf{x}, t) - \nabla \cdot D(\mathbf{x}, t) - D(\mathbf{x}, t) \nabla \log \hat{p}_t(\mathbf{x}; \theta^*).$$

Substituting this expression for \mathbf{u}_{θ^*} back into the continuity equation (4.17), we obtain:

$$(4.19) \quad \frac{\partial \hat{p}_t}{\partial t} = -\nabla \cdot \left\{ \hat{p}_t \left[\mathbf{f} - \nabla \cdot \mathbf{D} - \mathbf{D} \frac{\nabla \hat{p}_t}{\hat{p}_t} \right] \right\}$$

$$(4.20) \quad = -\nabla \cdot (\hat{p}_t \mathbf{f}) + \nabla \cdot (\hat{p}_t \nabla \cdot \mathbf{D}) + \nabla \cdot (\mathbf{D} \nabla \hat{p}_t).$$

Using the identity $\nabla \cdot (\nabla \cdot (\hat{p}_t \mathbf{D})) = \nabla \cdot (\hat{p}_t \nabla \cdot \mathbf{D}) + \nabla \cdot (\mathbf{D} \nabla \hat{p}_t)$, this simplifies to:

$$(4.21) \quad \frac{\partial \hat{p}_t}{\partial t} = -\nabla \cdot [\hat{p}_t \mathbf{f}] + \nabla \cdot \{ \nabla \cdot [\hat{p}_t \mathbf{D}] \},$$

which recovers the exact form of the FP equation. The uniqueness follows from the Existence and Uniqueness Theorem for SDEs [35] under Lipschitz conditions. \square

4.5.2. Wasserstein Error Bound. In practice, the residual is minimized to a small tolerance $\epsilon_{\mathcal{R}} > 0$. We now derive how this non-zero residual translates to the distributional error measured by the 2-Wasserstein distance (W_2). We adopt a Lagrangian perspective, analyzing the divergence of trajectories generated by the learned flow versus the true flow.

LEMMA 4.2 (Coupling Lemma). *Let μ_t and ν_t denote the probability measures associated with the true density $p_t(\cdot)$ and the approximated density $\hat{p}_t(\cdot)$, respectively. The 2-Wasserstein distance [50] is defined as:*

$$(4.22) \quad W_2^2(\mu_t, \nu_t) = \inf_{\pi \in \Pi(\mu_t, \nu_t)} \int_{\Omega \times \Omega} \|x - y\|^2 d\pi(x, y).$$

In our A-PFRM framework, both the true process X_t and the approximated process \hat{X}_t are pushed forward from the same initial distribution $X_0 \sim p_0$ via their respective ODEs derived from \mathbf{v}_t and $\hat{\mathbf{v}}_t$. The joint distribution of (X_t, \hat{X}_t) thus constitutes a valid synchronous coupling $\pi_{\text{flow}} \in \Pi(\mu_t, \nu_t)$. By the definition of the infimum, we immediately obtain the upper bound:

$$(4.23) \quad W_2^2(p_t, \hat{p}_t) = W_2^2(\mu_t, \nu_t) \leq \mathbb{E}_{(X_t, \hat{X}_t) \sim \pi_{\text{flow}}} [\|X_t - \hat{X}_t\|^2].$$

Furthermore, we need to introduce an inequality relation and the stability of the score function to lay the groundwork for subsequent theorem proofs:

LEMMA 4.3 (Differential Inequality Lemma). *Let $y(t)$ be a differentiable function on $[0, T]$, and satisfy the following differential inequality:*

$$(4.24) \quad y'(t) \leq \lambda y(t) + h(t), \quad \forall t \in [0, T],$$

where λ is a constant, $h(t)$ is a continuous function. If the initial condition satisfies $y(0) = 0$, then

$$(4.25) \quad y(t) \leq \int_0^t e^{\lambda(t-s)} h(s) ds.$$

Proof. By introducing an integrating factor $e^{-\lambda t}$ and rearranging the terms, we have

$$(4.26) \quad e^{-\lambda t} y'(t) - \lambda e^{-\lambda t} y(t) \leq e^{-\lambda t} h(t).$$

Notice that

$$(4.27) \quad \frac{d}{dt} [e^{-\lambda t} y(t)] = e^{-\lambda t} y'(t) + (-\lambda e^{-\lambda t}) y(t),$$

then

$$(4.28) \quad \frac{d}{dt} [e^{-\lambda t} y(t)] = e^{-\lambda t} y'(t) + (-\lambda e^{-\lambda t}) y(t) \leq e^{-\lambda t} h(t).$$

Integrate both sides of the inequality over the interval $[0, t]$ with respect to s , we have

$$(4.29) \quad \int_0^t \frac{d}{ds} [e^{-\lambda s} y(s)] ds \leq \int_0^t e^{-\lambda s} h(s) ds,$$

which is

$$(4.30) \quad e^{-\lambda t} y(t) = e^{-\lambda t} y(t) - e^0 y(0) \leq \int_0^t e^{-\lambda s} h(s) ds.$$

Thus

$$(4.31) \quad y(t) \leq e^{\lambda t} \int_0^t e^{-\lambda s} h(s) ds = \int_0^t e^{\lambda(t-s)} h(s) ds.$$

□

LEMMA 4.4 (Stability of the Score Function). *Assume that the true density p_t and the approximated density \hat{p}_t are both bounded in Ω , i.e., there exists a constant $\epsilon > 0$ such that for all $x \in \Omega$, $p_t \geq \epsilon$ and $\hat{p}_t \geq \epsilon$. And the score function of the true density $\nabla \log p_t$ is also bounded in Ω , i.e., there exists a constant $M > 0$ such that $\|\nabla \log p_t\|_\infty \leq M$. Then the score function error is linearly controlled by the density error:*

$$(4.32) \quad \|\nabla \log \hat{p}_t - \nabla \log p_t\|_{L^2} \leq C_\Omega \|\hat{p}_t - p_t\|_{H^1},$$

where constant C_Ω depends on the geometric constants ϵ and M .

Proof. Denote $\delta p_t = \hat{p}_t - p_t$, then we have

$$(4.33) \quad \nabla \log \hat{p}_t - \nabla \log p_t = \frac{\nabla p_t + \nabla(\delta p_t)}{\hat{p}_t} - \frac{\nabla p_t}{p_t},$$

$$(4.34) \quad = \frac{\nabla(\delta p_t)}{\hat{p}_t} + \nabla p_t \left(\frac{1}{\hat{p}_t} - \frac{1}{p_t} \right),$$

$$(4.35) \quad = \frac{\nabla(\delta p_t)}{\hat{p}_t} - (\nabla \log p_t) \frac{\delta p_t}{\hat{p}_t}.$$

Using the triangle inequality, we can get that

$$(4.36) \quad \|\nabla \log \hat{p}_t - \nabla \log p_t\|_{L^2} \leq \left\| \frac{\nabla(\delta p_t)}{\hat{p}_t} \right\|_{L^2} + \|(\nabla \log p_t) \frac{\delta p_t}{\hat{p}_t}\|_{L^2}.$$

Since $\hat{p}_t \geq \epsilon$, the first term satisfies

$$(4.37) \quad \left\| \frac{1}{\hat{p}_t} \nabla(\delta p_t) \right\|_{L^2} \leq \frac{1}{\epsilon} \|\nabla(\delta p_t)\|_{L^2}.$$

Since $\|\nabla \log p_t\|_\infty \leq M$, the second term satisfies

$$(4.38) \quad \|(\nabla \log p_t) \frac{1}{\hat{p}_t} \delta p_t\|_{L^2} \leq \|\nabla \log p_t\|_\infty \cdot \left\| \frac{1}{\hat{p}_t} \right\|_\infty \cdot \|\delta p_t\|_{L^2} \leq \frac{M}{\epsilon} \|\delta p_t\|_{L^2}.$$

Then we have

$$(4.39) \quad \|\nabla \log \hat{p}_t - \nabla \log p_t\|_{L^2} \leq \frac{1}{\epsilon} \|\nabla(\delta p_t)\|_{L^2} + \frac{M}{\epsilon} \|\delta p_t\|_{L^2}.$$

According to the standard definition of Sobolev spaces [14], the H^1 -norm is defined as $\|u\|_{H^1} = (\|u\|_{L^2}^2 + \|\nabla u\|_{L^2}^2)^{1/2}$. By the equivalence of norms, we can set $\|u\|_{H^1} \geq \frac{1}{C_0}(\|u\|_{L^2} + \|\nabla u\|_{L^2})$. Thus

$$(4.40) \quad \|\nabla \log \hat{p}_t - \nabla \log p_t\|_{L^2} \leq C_\Omega \cdot \|\delta p_t\|_{H^1} = C_\Omega \cdot \|\hat{p}_t - p_t\|_{H^1},$$

where constant $C_\Omega = C_0 \cdot \max(\frac{1}{\epsilon}, \frac{M}{\epsilon})$ depends on the ϵ and M . \square

REMARK 4.5 (Justification of assumptions). *The assumptions in Lemma 4.4 are inherent to the A-PFRM framework and not restrictive in practice:*

- *Strict Positivity:* As formulated in Eq.(4.5), the density \hat{p}_t generated by CNF is the product of a strictly positive initial distribution p_0 (otherwise, $\log p_0$ cannot be defined) and an exponential term. Thus, $\hat{p}_t > 0$ holds by construction, preventing singularities, and the same applies to p_t .
- *Boundedness:* According to the Regularity Theorem [14], the true density p_t becomes smooth C^∞ for any $t > 0$. Besides, the Strong Maximum Principle [14] guarantees that p_t remains strictly positive in the interior of the domain. These two properties combined—smoothness of ∇p_t and the strict lower bound of p_t on compact domains—ensure that the true score function $\nabla \log p_t = \nabla p_t / p_t$ is well-defined and bounded.

We now present the main theorem relating the training residual to the W_2 error.

THEOREM 4.6 (Error Bound via Residual). *Assume the drift function $\mathbf{f}(\mathbf{x}, t)$ and diffusion function $\mathbf{G}(\mathbf{x}, t)$ are Lipschitz-continuous with respect to \mathbf{x} , which implies the true probability flow velocity \mathbf{v}_t is L -Lipschitz, and the derived diffusion matrix $\mathbf{D}(\mathbf{x}, t) = \frac{1}{2}\mathbf{G}(\mathbf{x}, t)\mathbf{G}(\mathbf{x}, t)^T$ is uniformly elliptic (positive definite). Then for any $t \in [0, T]$, the W_2 distance between the true density $p_t(\cdot)$ and the approximated density $\hat{p}_t(\cdot)$ can be bounded:*

$$(4.41) \quad W_2(p_t, \hat{p}_t)^2 \leq \mathcal{L}_{\max}(t)(1 + K_{\text{score}})^2 \cdot \frac{e^{(2L+1)t} - 1}{2L + 1},$$

where K_{score} is a constant related to the activation function of neural network and the solution domain Ω , $\mathcal{L}_{\max}(t)$ represents the maximum A-PFRM loss at specific time τ within the time interval $\tau \in [0, t]$:

$$(4.42) \quad \mathcal{L}_{\max}(t) = \max_{\tau \in [0, t] \subset [0, T]} \mathcal{L}_{\text{Adapt}}(\theta, \tau) = \max_{\tau \in [0, t] \subset [0, T]} \mathbb{E}_{\hat{X}_\tau \sim \hat{p}_\tau} [\|\hat{\mathbf{v}}_\tau(\hat{X}_\tau) - \mathbf{u}_\theta(\hat{X}_\tau, \tau)\|^2].$$

Proof. Using Lemma 4.2, we can get that

$$(4.43) \quad W_2^2(p_t, \hat{p}_t) \leq \mathbb{E}_{(X_t, \hat{X}_t) \sim \pi_{\text{flow}}} [\|X_t - \hat{X}_t\|^2].$$

Since both the true PF-ODE and the approximated Neural ODE are deterministic given the initial state X_0 , the joint distribution at time t is fully determined by the initial distribution p_0 . By expressing the trajectories as flows $X_t = \Phi_{\text{true}}^t(X_0)$ and $\hat{X}_t = \Phi_\theta^t(X_0)$, we can rewrite the expectation over the coupling directly as an expectation over the initial condition:

$$(4.44) \quad \mathbb{E}_{(X_t, \hat{X}_t) \sim \pi_{\text{flow}}} [\|X_t - \hat{X}_t\|^2] \equiv \mathbb{E}_{X_0 \sim p_0} [\|\Phi_{\text{true}}^t(X_0) - \Phi_\theta^t(X_0)\|^2] = \mathbb{E}_{X_0 \sim p_0} [\|X_t - \hat{X}_t\|^2].$$

Consequently, the distributional error is strictly bounded by the mean squared error (MSE) of the Lagrangian trajectories:

$$(4.45) \quad W_2^2(p_t, \hat{p}_t) \leq \mathbb{E}_{X_0 \sim p_0} [\|X_t - \hat{X}_t\|^2].$$

Denote $E(t) = \mathbb{E}_{X_0 \sim p_0} [\|X_t - \hat{X}_t\|^2]$ be the MSE of trajectories at time t . Its time derivative is:

$$(4.46) \quad \frac{d}{dt} E(t) = \frac{d}{dt} \mathbb{E} [\|X_t - \hat{X}_t\|^2] = 2\mathbb{E} \left[\langle X_t - \hat{X}_t, \frac{d}{dt} X_t - \frac{d}{dt} \hat{X}_t \rangle \right].$$

By the definition of PF-ODE Eq.(4.3) and Neural ODE Eq.(4.4), we can substitute the ODE dynamics:

$$(4.47) \quad \frac{d}{dt} X_t = \mathbf{v}_t(X_t), \quad \frac{d}{dt} \hat{X}_t = \mathbf{u}_\theta(X_t, t).$$

Then we have

$$(4.48) \quad \frac{d}{dt} E(t) = 2\mathbb{E} \left[\langle X_t - \hat{X}_t, \mathbf{v}_t(X_t) - \mathbf{u}_\theta(\hat{X}_t) \rangle \right],$$

$$(4.49) \quad = 2\mathbb{E} \left[\langle X_t - \hat{X}_t, \underbrace{\mathbf{v}_t(X_t) - \mathbf{v}_t(\hat{X}_t)}_{\text{Lipschitz}} + \underbrace{\mathbf{v}_t(\hat{X}_t) - \mathbf{u}_\theta(\hat{X}_t)}_{\text{Velocity Mismatch}} \rangle \right].$$

Since $\mathbf{v}_t(\mathbf{x})$ is L -Lipschitz, then

$$(4.50) \quad \frac{d}{dt} E(t) \leq 2\mathbb{E} [\|X_t - \hat{X}_t\| \cdot L \|X_t - \hat{X}_t\|] + 2\mathbb{E} [\|X_t - \hat{X}_t\| \cdot \|\mathbf{v}_t(\hat{X}_t) - \mathbf{u}_\theta(\hat{X}_t)\|],$$

$$(4.51) \quad = 2L \cdot E(t) + 2\mathbb{E} [\|X_t - \hat{X}_t\| \cdot \|\delta(t)\|],$$

where $\delta(t) = \mathbf{v}_t(\hat{X}_t) - \mathbf{u}_\theta(\hat{X}_t)$ represents the instantaneous velocity mismatch error. Apply Young's Inequality ($2ab \leq a^2 + b^2$) yields:

$$(4.52) \quad 2\|X_t - \hat{X}_t\| \cdot \|\delta(t)\| \leq \|X_t - \hat{X}_t\|^2 + \|\delta(t)\|^2.$$

Thus

$$(4.53) \quad \frac{d}{dt} E(t) \leq 2L \cdot E(t) + E(t) + \mathbb{E} [\|\delta(t)\|^2] = (2L + 1)E(t) + \mathcal{L}_{true}(t),$$

here $\mathcal{L}_{true}(t) = \mathbb{E} [\|\delta(t)\|^2] = \mathbb{E} [\|\mathbf{v}_t(\hat{X}_t) - \mathbf{u}_\theta(\hat{X}_t)\|^2]$ corresponds to the squared velocity mismatch loss. By Lemma 4.3, with initial condition $E(0) = \mathbb{E}_{X_0 \sim p_0} [\|X_0 - \hat{X}_0\|^2] = 0$ (since $\hat{X}_0 = X_0 \sim p_0$), we have

$$(4.54) \quad E(t) \leq \int_0^t e^{(2L+1)(t-\tau)} \mathcal{L}_{true}(\tau) d\tau.$$

Define the $L_2(p)$ norm as

$$(4.55) \quad \|f\|_{\hat{p}_t}^2 = \mathbb{E}_{\hat{X}_t \sim \hat{p}_t} [\|f(\hat{X}_t)\|^2].$$

Then we have $\mathcal{L}_{true}(t) = \|\mathbf{u}_\theta - \mathbf{v}_t\|_{\hat{p}_t}^2$ and $\mathcal{L}_{Adapt}(\theta, t) = \|\mathcal{R}(\mathbf{x}, t; \theta)\|_{\hat{p}_t}^2 = \|\mathbf{u}_\theta - \hat{\mathbf{v}}_t\|_{\hat{p}_t}^2$. Using the triangle inequality

$$(4.56) \quad \underbrace{\|\mathbf{u}_\theta - \mathbf{v}_t\|_{\hat{p}_t}}_{\sqrt{\mathcal{L}_{true}}} \leq \underbrace{\|\mathbf{u}_\theta - \hat{\mathbf{v}}_t\|_{\hat{p}_t}}_{\sqrt{\mathcal{L}_{Adapt}(\theta, t)}} + \underbrace{\|\hat{\mathbf{v}}_t - \mathbf{v}_t\|_{\hat{p}_t}}_{\text{Score Error}},$$

where the Score Error term can be expanded as

$$(4.57) \quad \hat{\mathbf{v}}_t(\mathbf{x}) - \mathbf{v}_t(\mathbf{x}) = \mathbf{D}_t(\mathbf{x}) [\nabla \log p_t(\mathbf{x}) - \nabla \log \hat{p}_t(\mathbf{x})].$$

The continuity equation of \hat{p}_t is

$$(4.58) \quad \frac{\partial \hat{p}_t}{\partial t} + \nabla \cdot (\hat{p}_t \mathbf{u}_\theta) = 0.$$

We can substitute \mathbf{u}_θ with the residual $\mathcal{R}(\mathbf{x}, t; \theta) = \mathbf{u}_\theta(\mathbf{x}, t) - \hat{\mathbf{v}}_t(\mathbf{x})$

$$(4.59) \quad \frac{\partial \hat{p}_t}{\partial t} + \nabla \cdot [\hat{p}_t(\hat{\mathbf{v}}_t + \mathcal{R})] = 0,$$

which is

$$(4.60) \quad \mathcal{F}(\hat{p}_t) = \frac{\partial \hat{p}_t}{\partial t} + \nabla \cdot (\hat{p}_t \hat{\mathbf{v}}_t) = -\nabla \cdot (\hat{p}_t \mathcal{R}),$$

where \mathcal{F} is the FP equation operator. It means that \hat{p}_t is a solution to one FP equation with a source term (determined by the residual \mathcal{R}). And we know that p_t is a solution to the same FP equation without a source term, i.e., $\mathcal{F}(p_t) = 0$. The Stability Theorem of parabolic PDEs [14] shows that, with uniformly elliptic diffusion term $\mathbf{D}_t(\mathbf{x})$ and Lipschitz continuous drift term $\mathbf{f}_t(\mathbf{x})$, the difference between PDE solutions is controlled by the residual:

$$(4.61) \quad \|\hat{p} - p_t\|_{H^1} \leq C_{stab} \|\nabla \cdot (\hat{p} \mathcal{R})\|_{H^{-1}} \leq C'_{stab} \|\hat{p} \mathcal{R}\|_{L^2}.$$

Remark 4.5 shows that our A-PFRM framework inherently satisfies the assumptions of Lemma 4.4. Therefore, using Lemma 4.4 and the equivalence of norms, we can obtain

$$(4.62) \quad \|\hat{\mathbf{v}}_t - \mathbf{v}_t\|_{\hat{p}_t} = \left\| \mathbf{D}_t \left[\nabla \log p_t - \nabla \log \hat{p}_t \right] \right\|_{\hat{p}_t},$$

$$(4.63) \quad \leq \mathbf{D}_{max} \cdot C_1 \cdot \|\nabla \log \hat{p}_t - \nabla \log p_t\|_{L_2},$$

$$(4.64) \quad \leq \mathbf{D}_{max} \cdot C_1 \cdot C_\Omega \cdot \|\hat{p}_t - p_t\|_{H^1},$$

$$(4.65) \quad \leq \mathbf{D}_{max} \cdot C_1 \cdot C_\Omega \cdot C'_{stab} \|\hat{p} \mathcal{R}\|_{L^2}.$$

Since the velocity field \mathbf{u}_θ employs Tanh activation functions, which are smooth and bounded, the density \hat{p}_t evolved via CNF remains bounded on the solution domain Ω . We treat it as a finite constant C_{Tanh} . Then the Score Error can be bounded

$$(4.66) \quad \|\hat{\mathbf{v}}_t - \mathbf{v}_t\|_{\hat{p}_t} \leq \mathbf{D}_{max} \cdot C_1 \cdot C_\Omega \cdot C'_{stab} \cdot C_{\text{Tanh}} \cdot \|\mathcal{R}\|_{L_2},$$

$$(4.67) \quad \leq \mathbf{D}_{max} \cdot C_1 \cdot C_\Omega \cdot C'_{stab} \cdot C_{\text{Tanh}} \cdot C_2 \cdot \|\mathcal{R}\|_{\hat{p}_t},$$

$$(4.68) \quad = \mathbf{D}_{max} \cdot C_1 \cdot C_\Omega \cdot C'_{stab} \cdot C_{\text{Tanh}} \cdot C_2 \cdot \sqrt{\mathcal{L}_{\text{Adapt}}(\theta, t)},$$

$$(4.69) \quad \triangleq K_{score} \cdot \sqrt{\mathcal{L}_{\text{Adapt}}(\theta, t)}.$$

Thus we have

$$(4.70) \quad \underbrace{\|\mathbf{u}_\theta - \mathbf{v}_t\|_{\hat{p}_t}}_{\sqrt{\mathcal{L}_{true}}} \leq \underbrace{\|\mathbf{u}_\theta - \hat{\mathbf{v}}_t\|_{\hat{p}_t}}_{\sqrt{\mathcal{L}_{\text{Adapt}}(\theta, t)}} + \underbrace{\|\hat{\mathbf{v}}_t - \mathbf{v}_t\|_{\hat{p}_t}}_{\text{Score Error}} \leq (1 + K_{score}) \sqrt{\mathcal{L}_{\text{Adapt}}(\theta, t)},$$

which means

$$(4.71) \quad \mathcal{L}_{true}(t) \leq (1 + K_{score})^2 \cdot \mathcal{L}_{\text{Adapt}}(\theta, t).$$

Finally, we can get that

$$(4.72) \quad W_2^2(p_t, \hat{p}_t) \leq E(t) \leq \int_0^t e^{(2L+1)(t-\tau)} \mathcal{L}_{true}(\tau) d\tau,$$

$$(4.73) \quad \leq (1 + K_{score})^2 \int_0^t e^{(2L+1)(t-\tau)} \mathcal{L}_{Adapt}(\theta, \tau) d\tau,$$

$$(4.74) \quad \leq \mathcal{L}_{max}(t)(1 + K_{score})^2 \int_0^t e^{(2L+1)(t-\tau)} d\tau,$$

$$(4.75) \quad = \mathcal{L}_{max}(t)(1 + K_{score})^2 \cdot \frac{e^{(2L+1)t} - 1}{2L + 1},$$

where

$$(4.76) \quad \mathcal{L}_{max}(t) = \max_{\tau \in [0, t] \subset [0, T]} \mathcal{L}_{Adapt}(\theta, \tau) = \max_{\tau \in [0, t] \subset [0, T]} \mathbb{E}_{\hat{x}_\tau \sim \hat{p}_\tau} [\|\hat{\mathbf{v}}_\tau(\hat{X}_\tau) - \mathbf{u}_\theta(\hat{X}_\tau, \tau)\|^2].$$

□

REMARK 4.7 (Alignment between Theory and Algorithm). *Theorem 4.6 provides the rigorous justification for our generative adaptive sampling strategy. The error bound depends critically on the term $\mathcal{L}_{Adapt}(\theta, \tau) = \mathbb{E}_{\mathbf{x} \sim \hat{p}_\tau} [\|\mathcal{R}(\mathbf{x}, \tau; \theta)\|^2]$, which is the residual norm weighted by the generated density \hat{p}_τ .*

In high-dimensional spaces, the probability mass of \hat{p}_τ may be concentrated on a small manifold. Standard uniform sampling minimizes the residual over the entire domain Ω , which is mathematically mismatched with the \hat{p}_τ -weighted norm Eq.(4.55) required by the theory. A model could achieve low uniform loss by being accurate in empty regions while having large residuals on the actual probability flow paths, leading to divergent trajectories. The adaptive sampling strategy (Algorithm 1) explicitly generates samples $\mathbf{x} \sim \hat{p}_\tau$ to estimate this specific expectation, ensuring that the optimization objective aligns with the theoretical requirement for convergence.

5. Numerical Experiments. To validate the performance, accuracy, and scalability of our proposed A-PFRM method, we conduct a series of numerical experiments, including a one-dimensional Ornstein-Uhlenbeck (OU) process, a two-dimensional anisotropic OU process with rotational drift, a two-dimensional bimodal OU process, a high-dimensional Brownian motion with time-varying diffusion terms, and a high-dimensional geometric OU process. All numerical algorithms were implemented using the PyTorch framework [37]. All experiments were performed on an NVIDIA RTX 5090 GPU with 32GB memory.

For comparison, the time dependent flow-based generative model tKRnet [21] is considered. Due to its training paradigm, which relies on minimizing PDE residuals, it can be extended to solve FP equations by incorporating the second-order diffusion term into the loss function. Like the proposed A-PFRM, tKRnet employs an adaptive sampling strategy to optimize collocation points dynamically. However, a fundamental distinction remains in the optimization objective: tKRnet minimizes the violation of the instantaneous PDE residual (specifically, the logarithmic FP equation in this context), whereas our A-PFRM minimizes a probability flow loss Eq.(4.12) derived from the equivalent PF-ODE.

A significant challenge in ensuring a fair comparison arises from the inherent architectural disparities between the proposed method and the baseline. Our A-PFRM utilizes a compact Multi-Layer Perceptron (MLP) with 2 hidden layers to parameterize the velocity field $\mathbf{u}_\theta(\mathbf{x}, t)$. In contrast, the tKRnet $T(\mathbf{x}, t; \Theta)$ is a complex flow-based generative model constructed by composing K invertible transformation blocks based on the Knothe-Rosenblatt rearrangement [46]. While a conventional comparison might attempt to control for model

complexity by equalizing the number of trainable parameters, the tKRnet architecture inherently relies on deep, complex flow transformations to achieve high expressivity; artificially reducing its capacity to match a compact MLP would not reflect its intended design and performance capability. Therefore, to ensure a rigorous evaluation against a competitive baseline, we adopt the recommended network configurations for tKRnet, resulting in a considerably larger parameter count compared to our A-PFRM method. To account for this disparity, we explicitly report both the training time and the parameter quantity alongside accuracy metrics.

We assess the accuracy of the learned density $\hat{p}_t(\mathbf{x}; \theta)$ by comparing it to the true analytical solution $p_t(\mathbf{x})$ over a sequence of test timestamps $t \in \{t_{\text{test}}\}$. To ensure a unified and numerically robust evaluation framework across dimensions ranging from 1D to 100D, we adopt metrics based on the logarithm of the PDF. In high-dimensional spaces, probability density values often decay exponentially, leading to significant numerical underflow issues that render standard L_2 or L_∞ metrics on raw PDF values unreliable [24]. Operating in the logarithmic domain mitigates these floating-point limitations. For the sake of consistency, we apply these log-domain metrics to all test cases, including low-dimensional ones. Specifically, the metrics are defined as follows: For any given time instance t , we quantify the PDF differences using the following metrics:

- Kullback-Leibler (KL) Divergence and Relative KL Error:

The KL divergence is defined as follows:

(5.1)

$$D_{KL}(p_t(\mathbf{x}) \parallel \hat{p}_t(\mathbf{x}; \theta)) = \mathbb{E}_{\mathbf{x} \sim p_t} \left[\log \frac{p_t(\mathbf{x})}{\hat{p}_t(\mathbf{x}; \theta)} \right] = \int_{\mathbb{R}^d} p_t(\mathbf{x}) [\log p_t(\mathbf{x}) - \log \hat{p}_t(\mathbf{x}; \theta)] d\mathbf{x}.$$

It focuses on measuring the fitting effect of the model in the high-probability region. To further eliminate the influence of the dimension on the KL divergence value, we define the KL relative error:

$$(5.2) \quad \text{KL Rel.Err.} = \frac{D_{KL}(p_t(\mathbf{x}) \parallel \hat{p}_t(\mathbf{x}; \theta))}{H(p_t(\mathbf{x}))},$$

where $H(p_t(\mathbf{x})) = \mathbb{E}_{\mathbf{x} \sim p_t} [-\log p_t(\mathbf{x})]$ is the entropy of true distribution $p_t(\mathbf{x})$. In practice, we approximate the expectations using MC integration with samples drawn from the exact solution p_t :

$$(5.3) \quad \text{KL Rel.Err.} \approx \frac{\sum_{i=1}^{N_{\text{KL}}} (\log p_t(\mathbf{x}_i) - \log \hat{p}_t(\mathbf{x}_i; \theta))}{\sum_{i=1}^{N_{\text{KL}}} (-\log p_t(\mathbf{x}_i))}, \quad \mathbf{x}_i \sim p_t(\mathbf{x}),$$

where $N_{\text{KL}} = 2.0 \times 10^5$ is the sample size for validation.

- Relative L_2 Error of Log-Likelihood:

To evaluate the global fitting quality across the entire domain Ω while mitigating numerical issues associated with decaying PDF tails, we compute the relative L_2 error in the log-domain:

(5.4)

$$\text{LL } L_2 \text{ Rel.Err.} = \frac{\|\log p_t - \log \hat{p}_t\|_{L_2(\Omega)}}{\|\log p_t\|_{L_2(\Omega)}} = \frac{\left[\int_{\Omega} |\log p_t(\mathbf{x}) - \log \hat{p}_t(\mathbf{x}; \theta)|^2 d\mathbf{x} \right]^{1/2}}{\left[\int_{\Omega} |\log p_t(\mathbf{x})|^2 d\mathbf{x} \right]^{1/2}}.$$

This metric is approximated via MC integration using uniform sampling over the domain Ω :

$$(5.5) \quad \text{LL } L_2 \text{ Rel.Err.} \approx \sqrt{\frac{\sum_{i=1}^{N_L} |\log p_t(\mathbf{x}_i) - \log \hat{p}_t(\mathbf{x}_i; \theta)|^2}{\sum_{i=1}^{N_L} |\log p_t(\mathbf{x}_i)|^2}}, \quad \mathbf{x}_i \sim \text{Uniform}(\Omega),$$

where $N_L = 2.0 \times 10^5$ denotes the number of uniform validation samples.

- **Relative L_∞ Error of Log-Likelihood:**

The relative L_∞ error measures the worst-case point-wise discrepancy in the log-domain:

(5.6)

$$\text{LL } L_\infty \text{ Rel.Err.} = \frac{\|\log p_t - \log \hat{p}_t\|_{L_\infty(\Omega)}}{\|\log p_t\|_{L_\infty(\Omega)}} = \frac{\sup_{\mathbf{x} \in \Omega} |\log p_t(\mathbf{x}) - \log \hat{p}_t(\mathbf{x}; \theta)|}{\sup_{\mathbf{x} \in \Omega} |\log p_t(\mathbf{x})|}.$$

Similarly, this is estimated using the maximum values over a large set of uniform samples:

$$(5.7) \quad \text{LL } L_\infty \text{ Rel.Err.} \approx \frac{\max_i |\log p_t(\mathbf{x}_i) - \log \hat{p}_t(\mathbf{x}_i; \theta)|}{\max_i |\log p_t(\mathbf{x}_i)|}, \quad \mathbf{x}_i \sim \text{Uniform}(\Omega).$$

Given that the complexity of the probability density function evolves over time and the peak approximation errors may occur at different stages of the dynamics, evaluating the model at a single time point may not provide a comprehensive assessment. Therefore, unless otherwise specified, the quantitative results reported in the subsequent tables represent the temporal averages of the aforementioned metrics computed over the entire sequence of test time points $t \in \{t_{\text{test}}\}$:

$$(5.8) \quad \overline{\text{Err.}} = \frac{1}{N_t} \sum_{t \in \{t_{\text{test}}\}} \text{Err.}(t),$$

where N_t is the number of time snapshots in the test set, and $\text{Err.}(t)$ represents any of the three error metrics defined above at time t .

5.1. A one-dimensional test problem. We start with this one-dimensional case, where the original SDE is

$$(5.9) \quad dx_t = -x_t dt + \sqrt{2} dw_t, \quad X_0 \sim p_0 = \mathcal{N}(\mu_0 = 3, \sigma_0^2 = 0.2^2), \quad t \in [0, 2].$$

The FP equation governing the PDF evolution of above SDE is

$$(5.10) \quad \frac{\partial p_t(x)}{\partial t} = \frac{\partial}{\partial x} [x p_t(x)] + \frac{\partial^2 p_t(x)}{\partial x^2},$$

$$(5.11) \quad \int_{\mathbb{R}} p_t(x) dx = 1, \quad p_t(x) \geq 0, \quad \forall t \in [0, 2],$$

$$(5.12) \quad p_0(x) = \mathcal{N}(x; \mu_0 = 3, \sigma_0^2 = 0.2^2),$$

and the exact solution is

$$(5.13) \quad p_t(x) = \mathcal{N}(x; \mu_t = 3 \cdot e^{-t}, \sigma_t^2 = 1 - 0.96 \cdot e^{-2t}).$$

According to Eq.(4.1), we can obtain the velocity field of this one-dimensional problem:

$$(5.14) \quad v_t(x) = -x - \nabla \log p_t(x).$$

Hence, the loss function takes the form:

$$(5.15) \quad \mathcal{L}(\theta) = \mathbb{E}_{(\mathbf{x}, t) \sim \mathcal{D}} \left[\|u_\theta(\mathbf{x}, t) + \mathbf{x} + \nabla \log \hat{p}_t(\mathbf{x}; \theta)\|_2^2 \right],$$

where we set the initial sampling distribution $\mathcal{D}_0 = \text{Uniform}(\Omega \times [0, 2])$: domain of interest is $\Omega = [-5, 5]$ with sample batch size $N_x = 1024$ and the time schedule is $\{0.1 \cdot s\}_{s=1}^{20} \subset (0, 2]$.

We generate the initial parameters Θ_0 for the inputs of Algorithm 1, using Kaiming initialization [22] and construct a neural network $u_\theta(x, t)$ which contains 2 fully connected hidden layers with 64 neurons. The solver of the CNF-augmented ODE system is set to the 4-th order Runge-Kutta (RK-4) method with a step size of 0.05. The total number of training epochs is set to $N_{\text{epochs}} = 250$ with warm-up epochs $N_{\text{warmup}} = 100$ and ramp-up epochs $N_{\text{rampup}} = 100$. The final adaptive sampling ratio is set to $\alpha_{\text{adapt}} = 0.8$. The learning rate for Adam optimizer is set to $\eta = 0.001$. To comprehensively evaluate the model performance, we select a set of testing time snapshots $t_{\text{test}} = \{0.1, 0.5, 1.0, 1.5, 2.0\}$ for validation.

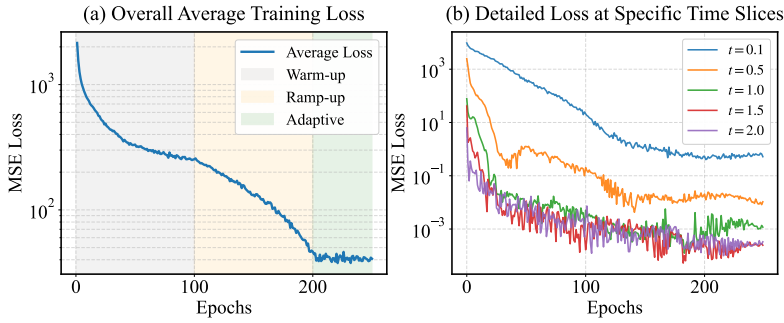


FIG. 5.1. Loss convergence during the training process, one-dimensional test problem.

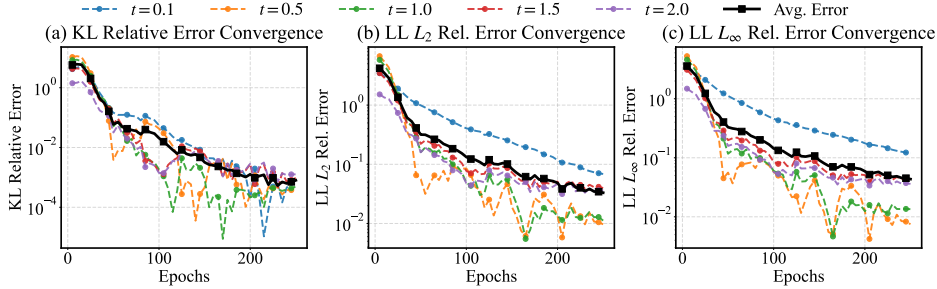


FIG. 5.2. Error convergence during the training process, one-dimensional test problem.

The training dynamics are illustrated in Fig. 5.1, where the average loss curve exhibits distinct convergence patterns corresponding to the three sampling stages (warm-up, ramp-up, and adaptive). Fig. 5.2 further details the convergence of PDF fitting errors across three metrics. Qualitatively, as shown in Fig. 5.3, while both methods accurately approximate the near-steady-state distributions ($t \geq 1.0$), the proposed A-PFRM method demonstrates superior precision during the rapid transient phase ($t = 0.1, 0.5$). Specifically, A-PFRM effectively captures the sharp peak evolution, whereas the baseline tKNet exhibits noticeable deviations in resolving these transient features. This performance gap is confirmed quantitatively in Table 5.1: A-PFRM achieves a KL relative error of 5.274×10^{-4} , which is two orders of magnitude lower than that of the baseline (5.036×10^{-2}), while requiring less than 4% of the model parameters and reducing the training time by over 50%.

Additionally, we utilize this tractable 1D benchmark to empirically verify the posterior error bound derived in Theorem 4.6. Specifically, since the exact solution p_t is a Gaussian

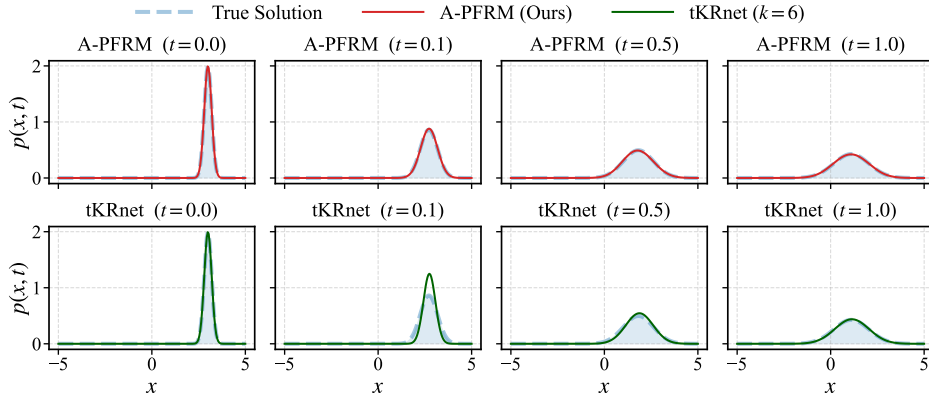


FIG. 5.3. Exact solution, A-PFRM solution (top) and tKRnet solution (bottom), one-dimensional test problem.

TABLE 5.1
Results for one-dimensional test problem.

Method	KL Rel. Err.	LL L_2 Rel. Err.	LL L_∞ Rel. Err.	Total Epochs	Time per Epoch (s)	Total Time (s)	# Parameters
tKRnet ($k = 3$)	8.223E-2	3.573E-1	3.642E-1	3×200	4.79	2,874	126,824
tKRnet ($k = 6$)	5.036E-2	3.427E-1	3.516E-1	6×200	4.79	5,746	126,824
A-PFRM	4.658E-4	3.373E-2	4.487E-2	250	11.15	2,787	4,417

distribution $\mathcal{N}(\mu_t, \sigma_t^2)$, and the approximated density \hat{p}_t closely follows a Gaussian profile, we can evaluate the 2-Wasserstein distance using the closed-form expression for univariate normal distributions:

$$(5.16) \quad W_2^2(p_t, \hat{p}_t) \approx (\mu_t - \hat{\mu}_t)^2 + (\sigma_t - \hat{\sigma}_t)^2,$$

where $\hat{\mu}_t$ and $\hat{\sigma}_t$ are estimated from the samples generated by the flow. We explicitly track the relationship between this error metric and the maximum A-PFRM residual $\mathcal{L}_{\max}(t)$ during the training phase. It is worth noting that to strictly align the numerical setup in Theorem 4.6 (where the expectation is defined solely over the generated density \hat{p}_t), we employed a pure adaptive sampling strategy for this specific verification task. The warm-up and ramp-up phases, as well as the uniform sampling component used in the standard Algorithm 1 for robustness, were excluded. This ensures that the computed residual $\mathcal{L}_{\max}(t)$ corresponds exactly to the \hat{p}_t -weighted norm required by the theory.

Figure 5.4 presents the verification results at two representative timestamps, $t = 1.0$ (intermediate phase) and $t = 2.0$ (terminal phase). As illustrated in Panel (a), the convergence trend of the A-PFRM residual (blue dashed line) exhibits a strong synchronization with that of the true W_2 error (red solid line). The simultaneous decay of both metrics empirically confirms that minimizing the probability flow residual effectively drives the distribution towards the true solution. Furthermore, Panel (b) visualizes the correlation between the error and the residual in a log-log scale. The solid black line represents the theoretical order of $1/2$ (i.e., $W_2 \propto \sqrt{\mathcal{L}}$) derived in Theorem 4.6. It is observed that the empirical slopes, indicated by the dashed red lines, are consistently steeper than the theoretical lower bound of 0.5 (e.g., 1.41 at $t = 1.0$ and 0.97 at $t = 2.0$). This indicates that the practical convergence rate surpasses the worst-case theoretical prediction, further validating the effectiveness and robustness of the

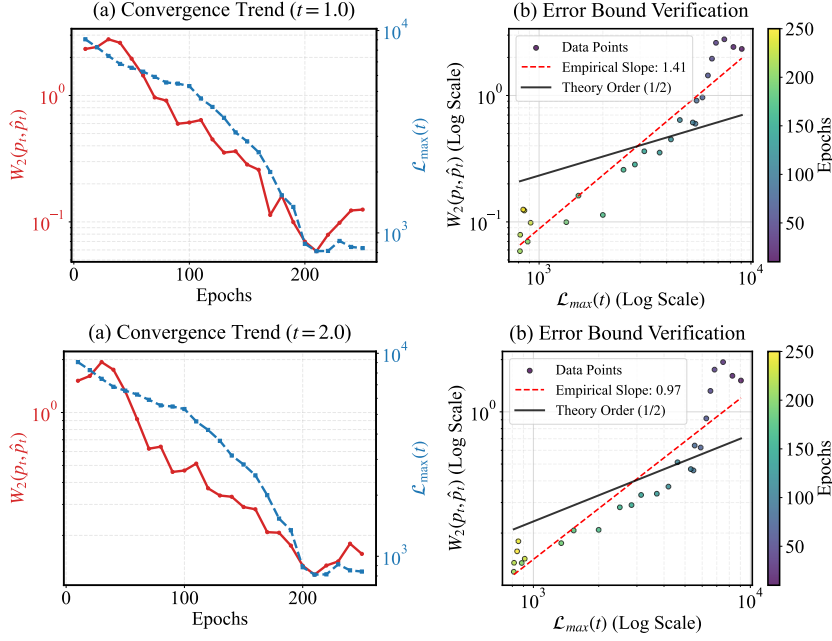


FIG. 5.4. Numerical verification of the error bound at $t = 1.0$ and $t = 2.0$. (a) The convergence trend shows correlation between the true W_2 error and the A-PFRM residual. (b) The log-log W_2 - \mathcal{L}_{\max} plot confirms that the empirical error decay rate (dashed red line) satisfies and exceeds the theoretical order of $1/2$ (black solid line).

proposed A-PFRM framework.

5.2. Two-dimensional test problems. In this subsection, we consider the two-dimensional FP equations, where the solution to the first problem is unimodal and the solution to the second problem is bimodal.

5.2.1. Two-dimensional unimodal test problem. The general SDE form of a multi-dimensional OU process is

$$(5.17) \quad dX_t = \mathbf{f}(X_t)dt + \mathbf{G}(X_t)dW_t, \quad X_0 \sim p_0 = \mathcal{N}(\boldsymbol{\mu}_0, \boldsymbol{\Sigma}_0), \quad t \in [0, 2].$$

In this test problem, we set the drift term $\mathbf{f} = -\mathbf{A}(X_t - \mathbf{c})$ to induce rotation, and the diffusion term \mathbf{G} to have anisotropic coupled noise:

$$(5.18) \quad \mathbf{A} = \begin{bmatrix} 0.5 & 1.5 \\ -1.0 & 1.0 \end{bmatrix}, \quad \mathbf{c} = \begin{bmatrix} 3.0 \\ 2.0 \end{bmatrix}, \quad \mathbf{G} = \begin{bmatrix} 1.0 & 0.7 \\ 0.0 & 0.5 \end{bmatrix}, \quad \mathbf{D} = \frac{1}{2}\mathbf{G}\mathbf{G}^T = \begin{bmatrix} 0.745 & 0.175 \\ 0.175 & 0.125 \end{bmatrix}.$$

The corresponding FP equation for this test problem is

$$(5.19) \quad \frac{\partial p_t(\mathbf{x})}{\partial t} = -\nabla \cdot [\mathbf{f}(\mathbf{x})p_t(\mathbf{x})] + \sum_{i,j=1}^2 \frac{\partial^2}{\partial x_i \partial x_j} [D_{ij}(\mathbf{x})p_t(\mathbf{x})],$$

$$(5.20) \quad \int_{\mathbb{R}^2} p_t(\mathbf{x}) = 1, \quad p_t(\mathbf{x}) \geq 0, \quad \forall t \in [0, 2],$$

$$(5.21) \quad p_0(\mathbf{x}) = \mathcal{N}(\mathbf{x}; \boldsymbol{\mu}_0 = \begin{bmatrix} -3.0 \\ -3.0 \end{bmatrix}, \boldsymbol{\Sigma}_0 = \begin{bmatrix} 3.0 & -1.8 \\ -1.8 & 2.0 \end{bmatrix}),$$

and the exact solution is

$$(5.22) \quad p_t(\mathbf{x}) = \mathcal{N}(\mathbf{x}; \boldsymbol{\mu}_t, \boldsymbol{\Sigma}_t), \quad \boldsymbol{\mu}_t = \mathbf{c} + e^{-At}(\boldsymbol{\mu}_0 - \mathbf{c}), \quad \boldsymbol{\Sigma}_t = \boldsymbol{\Sigma}_\infty - e^{-At}(\boldsymbol{\Sigma}_\infty - \boldsymbol{\Sigma}_0)e^{-A^T t},$$

where $\boldsymbol{\Sigma}_\infty$ is determined by the following continuous-time Lyapunov Equation

$$(5.23) \quad A\boldsymbol{\Sigma}_\infty + \boldsymbol{\Sigma}_\infty A^T = 2D.$$

The velocity field of this two-dimensional unimodal problem is

$$(5.24) \quad \mathbf{v}_t(\mathbf{x}) = -A(\mathbf{x} - \mathbf{c}) - D\nabla \log p_t(\mathbf{x}),$$

hence the loss function takes the form:

$$(5.25) \quad \mathcal{L}(\theta) = \mathbb{E}_{(\mathbf{x}, t) \sim \mathcal{D}} \left[\|\mathbf{u}_\theta(\mathbf{x}, t) + A(\mathbf{x} - \mathbf{c}) + D\nabla \log \hat{p}_t(\mathbf{x}; \theta)\|_2^2 \right],$$

where the initial sampling distribution $\mathcal{D}_0 = \text{Uniform}(\Omega \times [0, 2])$: domain of interest is $\Omega = [-10, 10]$ with sample batch size $N_x = 1024$ and the time schedule is $\{0.1 \cdot s\}_{s=1}^{20} \subset (0, 2]$.

We generate the initial parameters Θ_0 with Kaiming initialization and construct a neural network which contains 2 fully connected hidden layers with 128 neurons. The solver of the CNF-augmented ODE system is again set to the RK-4 method with a step size of 0.05. The total number of training epochs is set to $N_{\text{epochs}} = 500$ with warm-up epochs $N_{\text{warmup}} = 150$ and ramp-up epochs $N_{\text{rampup}} = 150$. The final adaptive sampling ratio is set to $\alpha_{\text{adapt}} = 0.8$. The learning rate for Adam optimizer is set to $\eta = 0.0005$. Consistent with the one-dimensional case, we select the test time snapshots $t_{\text{test}} = \{0.1, 0.5, 1.0, 1.5, 2.0\}$ for validation.

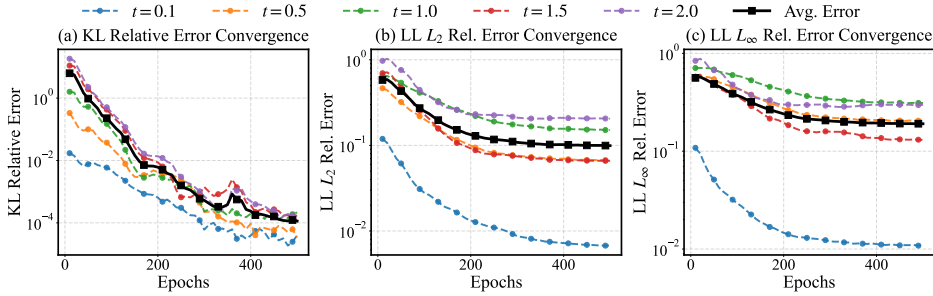


FIG. 5.5. Error convergence during the training process, two-dimensional unimodal test problem.

Fig. 5.5 shows the convergence history of the validation error. Fig. 5.6 presents a visual comparison of the density evolution at representative timestamps. Both methods capture the general anisotropic diffusion characteristics induced by the rotational drift and coupled diffusion matrix. However, the quantitative results in Table 5.2 reveal a substantial difference in approximation accuracy. While the gaps in global LL L_2 and LL L_∞ errors are moderate, the A-PFRM method achieves a KL relative error of 1.143×10^{-4} , nearly two orders of magnitude lower than the fully trained tKRnet (9.675×10^{-3}). In terms of computational efficiency, A-PFRM reduces the total training time by approximately 27% compared to the baseline, while utilizing only 13.6% of the parameter count (17k vs. 127k), demonstrating a higher accuracy-to-cost ratio.

5.2.2. Two-dimensional bimodal test problem. We increase the complexity of the problem by setting the initial distribution p_0 as a Gaussian Mixture Model (GMM). The

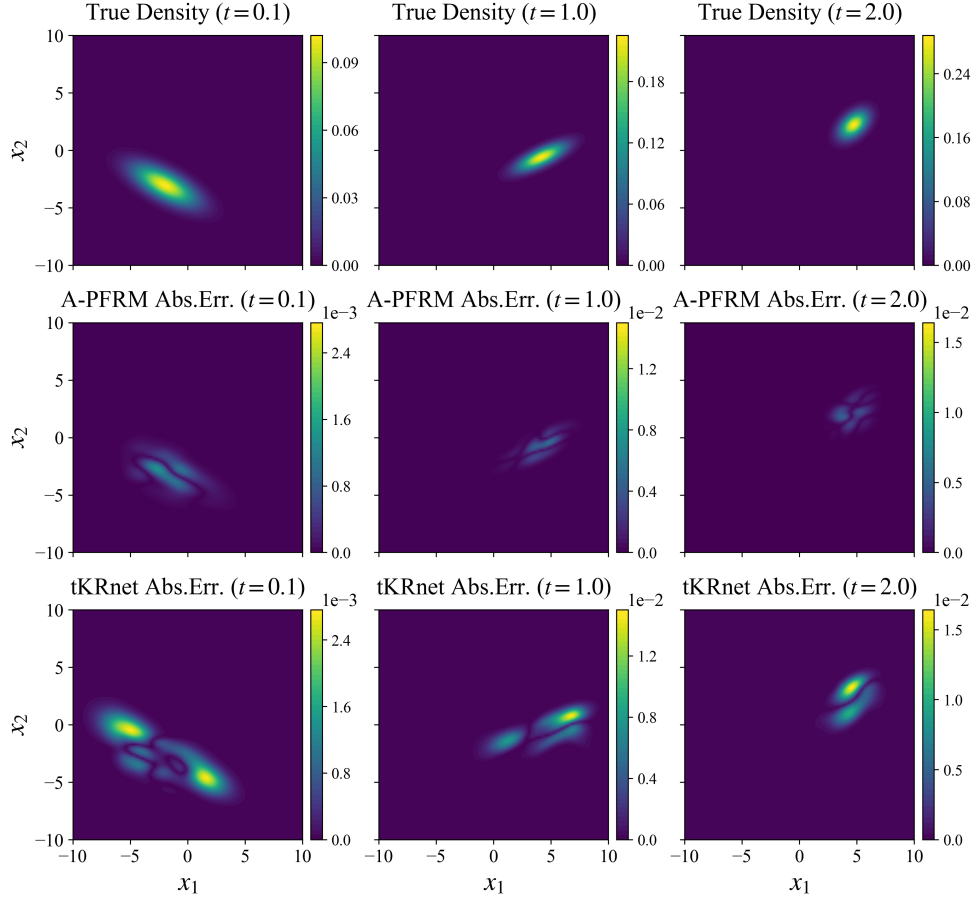


FIG. 5.6. Exact solution, A-PFRM Abs.Error and tKRnet Abs.Error, two-dimensional unimodal test problem.

TABLE 5.2
Results for two-dimensional unimodal test problem.

Method	KL Rel. Err.	LL L_2 Rel. Err.	LL L_∞ Rel. Err.	Total Epochs	Time per Epoch (s)	Total Time (s)	# Parameters
tKRnet ($k = 3$)	1.576E-2	6.251E-1	7.781E-1	3×200	8.56	5,136	127,528
tKRnet ($k = 6$)	9.675E-3	6.144E-1	7.806E-1	6×200	8.56	10,272	127,528
A-PFRM	1.143E-4	9.920E-2	1.908E-1	500	15.07	7,535	17,282

general SDE form remains:

$$(5.26) \quad dX_t = f(X_t)dt + G(X_t)dW_t, \quad X_0 \sim p_0 = \sum_{k=1}^2 w_k \mathcal{N}(\mu_{k,0}, \Sigma_{k,0}), \quad t \in [0, 2].$$

In this test problem, we set the drift term $\mathbf{f} = -\mathbf{A}(X_t - \mathbf{c})$ to have rotation, and the diffusion term \mathbf{G} to have simple anisotropic noise:

(5.27)

$$\mathbf{A} = \begin{bmatrix} 0.5 & 1.0 \\ -1.0 & 0.5 \end{bmatrix}, \quad \mathbf{c} = \begin{bmatrix} 0.0 \\ 0.0 \end{bmatrix}, \quad \mathbf{G} = \begin{bmatrix} 0.5 & 0.0 \\ 0.0 & 0.2 \end{bmatrix}, \quad \mathbf{D} = \frac{1}{2} \mathbf{G} \mathbf{G}^T = \begin{bmatrix} 0.125 & 0.0 \\ 0.0 & 0.02 \end{bmatrix},$$

The corresponding FP equation for this separable OU process is

$$(5.28) \quad \frac{\partial p_t(\mathbf{x})}{\partial t} = -\nabla \cdot [\mathbf{f}(\mathbf{x}) p_t(\mathbf{x})] + \sum_{i,j=1}^2 \frac{\partial^2}{\partial x_i \partial x_j} [D_{ij}(\mathbf{x}) p_t(\mathbf{x})],$$

$$(5.29) \quad \int_{\mathbb{R}^2} p_t(\mathbf{x}) = 1, \quad p_t(\mathbf{x}) \geq 0, \quad \forall t \in [0, 2],$$

$$(5.30) \quad p_0(\mathbf{x}) = \sum_{k=1}^2 w_k \mathcal{N}(\mathbf{x}; \boldsymbol{\mu}_{k,0}, \boldsymbol{\Sigma}_{k,0}), \quad w_1 = w_2 = 0.5,$$

where the initial components are

$$(5.31) \quad \boldsymbol{\mu}_{1,0} = \begin{bmatrix} 3.0 \\ -3.0 \end{bmatrix}, \quad \boldsymbol{\Sigma}_{1,0} = \begin{bmatrix} 0.5 & 0.3 \\ 0.3 & 0.5 \end{bmatrix}, \quad \boldsymbol{\mu}_{2,0} = \begin{bmatrix} -3.0 \\ 3.0 \end{bmatrix}, \quad \boldsymbol{\Sigma}_{2,0} = \begin{bmatrix} 0.7 & -0.5 \\ -0.5 & 1.0 \end{bmatrix}.$$

The exact solution $p_t(\mathbf{x})$ remains a GMM with constant weights, where each component evolves independently:

$$(5.32) \quad p_t(\mathbf{x}) = \sum_{k=1}^2 w_k \mathcal{N}(\mathbf{x}; \boldsymbol{\mu}_{k,t}, \boldsymbol{\Sigma}_{k,t}),$$

where

$$(5.33) \quad \boldsymbol{\mu}_{k,t} = \mathbf{c} + e^{-\mathbf{A}t}(\boldsymbol{\mu}_{k,0} - \mathbf{c}), \quad \boldsymbol{\Sigma}_{k,t} = \boldsymbol{\Sigma}_{\infty} - e^{-\mathbf{A}t}(\boldsymbol{\Sigma}_{\infty} - \boldsymbol{\Sigma}_{k,0})e^{-\mathbf{A}^T t},$$

and $\boldsymbol{\Sigma}_{\infty}$ is determined by the following continuous-time Lyapunov Equation

$$(5.34) \quad \mathbf{A} \boldsymbol{\Sigma}_{\infty} + \boldsymbol{\Sigma}_{\infty} \mathbf{A}^T = 2\mathbf{D}.$$

The velocity field and the loss function take the same form as the unimodal case, substituting the corresponding $\mathbf{A}, \mathbf{c}, \mathbf{D}$:

$$(5.35) \quad \mathbf{v}_t(\mathbf{x}) = -\mathbf{A}(\mathbf{x} - \mathbf{c}) - \mathbf{D} \nabla \log p_t(\mathbf{x}),$$

$$(5.36) \quad \mathcal{L}(\theta) = \mathbb{E}_{(\mathbf{x},t) \sim \mathcal{D}} \left[\|\mathbf{u}_{\theta}(\mathbf{x}, t) + \mathbf{A}(\mathbf{x} - \mathbf{c}) + \mathbf{D} \nabla \log \hat{p}_t(\mathbf{x}; \theta)\|_2^2 \right],$$

where the initial sampling distribution $\mathcal{D}_0 = \text{Uniform}(\Omega \times [0, 2])$: domain of interest is $\Omega = [-6, 6]^2$ with sample batch size $N_x = 1024$ and the time schedule is $\{0.1 \cdot s\}_{s=1}^{20} \subset (0, 2]$.

We use the same initialization and ODE solver as the unimodal case, but expand the scale of neural network, which contains 2 fully connected hidden layers with 256 neurons. The total number of training epochs is set to $N_{\text{epochs}} = 500$ with warm-up epochs $N_{\text{warmup}} = 150$ and ramp-up epochs $N_{\text{rampup}} = 150$. The final adaptive sampling ratio is set to $\alpha_{\text{adapt}} = 0.8$. The learning rate for Adam optimizer is set to $\eta = 0.0001$. We select the same test time snapshots $t_{\text{test}} = \{0.1, 0.5, 1.0, 1.5, 2.0\}$ for result evaluation.

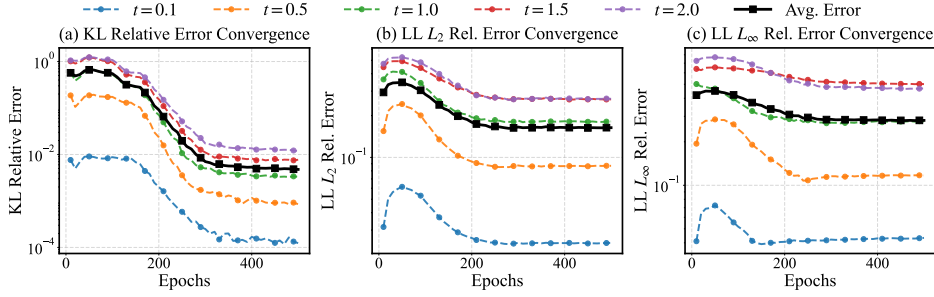


FIG. 5.7. Error convergence during the training process, two-dimensional bimodal test problem.

Fig. 5.7 illustrates the convergence of validation errors throughout the training process. Fig. 5.8 provides a visual comparison of the predicted density evolution, where both methods successfully resolve the separation and evolution of the two Gaussian components. Further numerical comparisons are shown in Table 5.3: our A-PFRM reduces the global LL L_2 and LL L_∞ errors by factors of approximately 2.4 and 2.0, respectively, compared to the baseline. Furthermore, this precision is attained with improved efficiency, where A-PFRM achieves a 1.8 times speedup in total training time while employing a model architecture that is nearly 50% more compact than the tKRnet baseline (67k vs. 127k parameters).

TABLE 5.3
Results for two-dimensional bimodal test problem.

Method	KL Rel. Err.	LL L_2 Rel. Err.	LL L_∞ Rel. Err.	Total Epochs	Time per Epoch (s)	Total Time (s)	# Parameters
tKRnet ($k = 3$)	7.179E-3	4.319E-1	6.191E-1	3×200	10.72	6,432	127,528
tKRnet ($k = 6$)	5.669E-3	3.998E-1	5.647E-1	6×200	10.72	12,864	127,528
A-PFRM	4.322E-3	1.612E-1	2.784E-1	500	14.21	7,105	67,330

5.3. High-dimensional test problems with time-varying diffusion terms. Following the experimental setup in [24], we consider a high-dimensional benchmark problem characterized by time-varying diffusion terms. As highlighted in [24], this problem poses a significant challenge because the evolving eigenspace of the diffusion matrix prevents the system from being simplified into isotropic or lower-dimensional sub-problems. The dynamics are governed by the following SDE:

$$(5.37) \quad dX_t = \mathbf{G}(t)dW_t, \quad X_0 \sim p_0 = \mathcal{N}(\mathbf{0}, \mathbf{I}), \quad t \in [0, 2].$$

Here, to better illustrate the difficulties introduced by the time-varying diffusion terms, we also set the drift term $\mathbf{f} = \mathbf{0}$, i.e., it is a Brownian Motion. The diffusion term is set to $\mathbf{G}(t) = \mathbf{B} + t\mathbf{I}$, hence the resulting diffusion matrix $\mathbf{D}(t)$ is also time-dependent:

$$(5.38) \quad \mathbf{D}(t) = \frac{1}{2}\mathbf{G}(t)\mathbf{G}(t)^T = \frac{1}{2}(\mathbf{B} + t\mathbf{I})(\mathbf{B} + t\mathbf{I})^T,$$

where \mathbf{B} is a constant matrix randomly constructed via QR decomposition to ensure anisotropy, as detailed in [24]. The corresponding FP equation for this test problem simplifies to a tran-

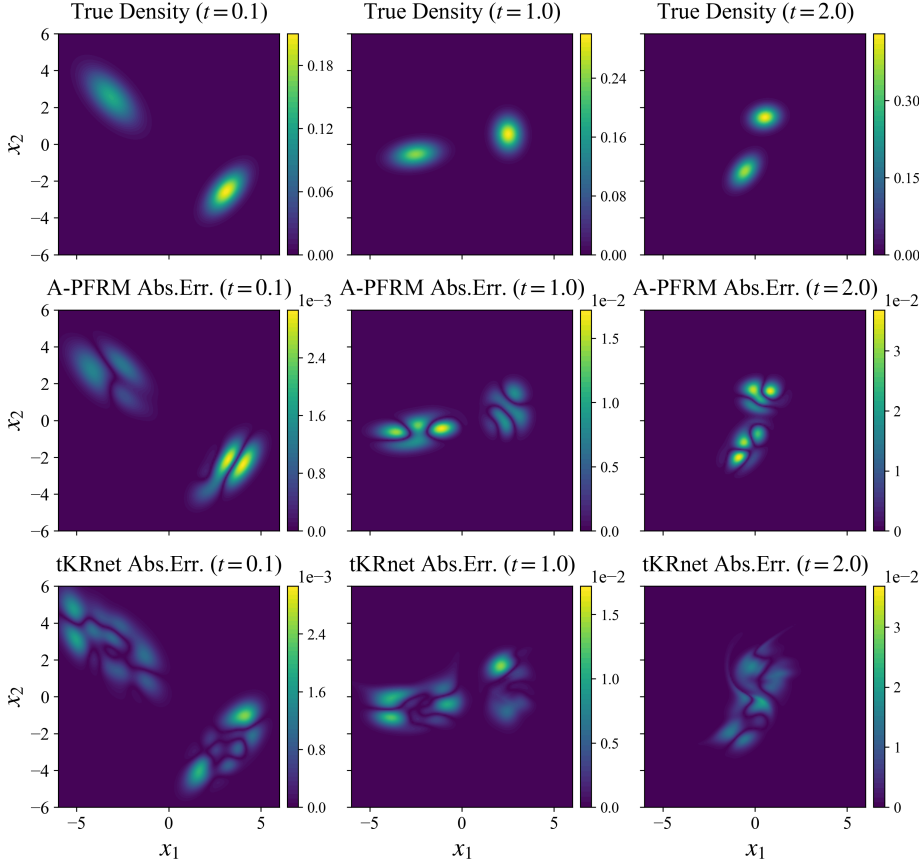


FIG. 5.8. Exact solution, A-PFRM Abs.Error and tKRnet Abs.Error, two-dimensional bimodal test problem.

sient diffusion equation with a time-varying tensor:

$$(5.39) \quad \frac{\partial p_t(\mathbf{x})}{\partial t} = \sum_{i,j=1}^d D_{ij}(t) \frac{\partial^2 p_t(\mathbf{x})}{\partial x_i \partial x_j},$$

$$(5.40) \quad \int_{\mathbb{R}^d} p_t(\mathbf{x}) = 1, \quad p_t(\mathbf{x}) \geq 0, \quad \forall t \in [0, 2],$$

$$(5.41) \quad p_0(\mathbf{x}) = \mathcal{N}(\mathbf{x}; \boldsymbol{\mu}_0 = \mathbf{0}, \boldsymbol{\Sigma}_0 = \mathbf{I}).$$

The exact solution remains Gaussian, $p_t(\mathbf{x}) = \mathcal{N}(\mathbf{x}; \mathbf{0}, \boldsymbol{\Sigma}_t)$, where the covariance matrix $\boldsymbol{\Sigma}_t$ evolves according to:

$$(5.42) \quad \boldsymbol{\Sigma}_t = \boldsymbol{\Sigma}_0 + \int_0^t 2\mathbf{D}(s)ds = \mathbf{I} + \int_0^t (\mathbf{B} + s\mathbf{I})(\mathbf{B} + s\mathbf{I})^T ds,$$

$$(5.43) \quad = \left(1 + \frac{t^3}{3}\right)\mathbf{I} + t\mathbf{B}\mathbf{B}^T + \frac{t^2}{2}(\mathbf{B} + \mathbf{B}^T).$$

The velocity field for this time-varying Brownian Motion problem is

$$(5.44) \quad \mathbf{v}_t(\mathbf{x}) = -\mathbf{D}(t)\nabla \log p_t(\mathbf{x}).$$

The loss function, consistent with the previous sections, targets this velocity:

$$(5.45) \quad \mathcal{L}(\theta) = \mathbb{E}_{(\mathbf{x}, t) \sim \mathcal{D}} \left[\|\mathbf{u}_\theta(\mathbf{x}, t) + \mathbf{D}(t)\nabla \log \hat{p}_t(\mathbf{x}; \theta)\|_2^2 \right],$$

where the initial sampling distribution $\mathcal{D}_0 = \text{Uniform}(\Omega \times [0, 2])$: domain of interest is $\Omega = [-13, 13]^d$ with sample batch size $N_x = 1024$ and the time schedule is $\{0.1 \cdot s\}_{s=1}^{20} \subset (0, 2]$.

For moderately high-dimensional test problems $d = 4, 8, 12$, we use the same network architecture as the two-dimensional cases, containing 2 fully connected hidden layers with 128 neurons and Θ_0 are initialized by Kaiming initialization. The solver of the CNF-augmented ODE system is set to the RK-4 method with a step size of 0.05. The total number of training epochs is set to $N_{\text{epoch}} = 500$ with warm-up epochs $N_{\text{warmup}} = 150$ and ramp-up epochs $N_{\text{rampup}} = 150$. The final adaptive sampling ratio is set to $\alpha_{\text{adapt}} = 0.8$. The learning rate for Adam optimizer is set to $\eta = 0.001$. We still select the test time snapshots $t_{\text{test}} = \{0.1, 0.5, 1.0, 1.5, 2.0\}$ for performance evaluation.

TABLE 5.4
Results for 4D, 8D, and 12D test problems with time-varying diffusion terms.

Dimension	4D		8D		12D	
	tKRnet	A-PFRM	tKRnet	A-PFRM	tKRnet	A-PFRM
KL Rel. Err.	1.220E-2	9.450E-6	1.450E-1	2.887E-5	–	1.107E-3
LL L_2 Rel. Err.	1.901E-1	6.552E-3	2.823E-1	8.563E-3	–	4.816E-2
LL L_∞ Rel. Err.	3.147E-1	1.954E-2	4.742E-1	2.832E-2	–	6.698E-2
Total Epochs	6×200	500	6×200	500	6×200	500
Time per Epoch (s)	18.09	20.57	79.42	24.58	190.32	32.98
Total Time (s)	21,708	10,286	95,304	12,292	–	16,490
# Parameters	385,531	17,796	913,597	18,824	1,457,743	19,852

* tKRnet results are reported using $k = 6$ iterations.

– Indicates training was not completed due to excessive computational cost.

Table 5.4 presents the comparative results for $d = 4, 8, 12$, aiming to evaluate the scalability of the methods as dimensionality increases. The baseline tKRnet encounters significant computational bottlenecks in this regime due to the $O(D^2)$ complexity of the second-order derivative terms. For the 8D case, tKRnet requires over 26 hours (95,304s) to complete training. In the 12D case, the training time per epoch escalates to 190.32s; consequently, the full training results for tKRnet are not reported (indicated by –). In contrast, the A-PFRM method maintains computational tractability. It completes the 12D training in approximately 4.5 hours (16,490 s). Regarding accuracy, A-PFRM outperforms the baseline in both 4D and 8D cases, achieving KL relative errors in the order of 10^{-5} , which are 3 to 4 orders of magnitude lower than those of tKRnet. In the 12D case, A-PFRM retains a KL relative error of 1.107×10^{-3} , confirming its capability to mitigate the CoD in this regime.

For higher-dimensional test problems $d = 20, 40, 60, 100$, we expand the scale of the neural network, which contains 2 fully connected hidden layers with 256 neurons. The network initialization and ODE solver are consistent with the setting in the $d = 4, 8, 12$ test problems. For these higher-dimensional problems, computing the exact divergence via automatic differentiation during the computation of CNF augmented ODE incurs significant computational costs. To address this, we employ the HTE Eq.(3.4) to quickly generate unbiased estimates of the exact divergence. The total number of training epochs is set to $N_{\text{epoch}} = 800$ with warm-up epochs $N_{\text{warmup}} = 200$ and ramp-up epochs $N_{\text{rampup}} = 200$. The final adaptive sampling ratio

is set to $\alpha_{\text{adapt}} = 0.8$. The learning rate for Adam optimizer is set to $\eta = 0.0005$. The test time snapshots $t_{\text{test}} = \{0.1, 0.5, 1.0, 1.5, 2.0\}$ remain the same.

TABLE 5.5
Results for 20D, 40D, 60D and 100D test problems with time-varying diffusion terms.

Dimension	20D	40D	60D	100D
Method	A-PFRM with HTE			
KL Rel. Err.	7.787E-4	7.537E-4	9.938E-4	1.169E-3
LL L_2 Rel. Err.	3.298E-2	3.097E-2	3.229E-2	3.303E-2
LL L_∞ Rel. Err.	5.814E-2	4.955E-2	4.965E-2	5.056E-2
Total Epochs	800	800	800	800
Time per Epoch (s)	11.97	11.89	11.94	11.96
Total Time (s)	9,576	9,512	9,552	9,568
# Parameters	76,564	86,824	97,084	117,604

Table 5.5 summarizes the results for dimensions up to 100, where A-PFRM is augmented with the HTE to handle high-dimensional divergence. A key observation is the relationship between training time and dimensionality. As the dimension increases five-fold from 20D to 100D, the average wall-clock time per epoch remains nearly constant at approximately 12 seconds. This dimension-independent computational cost (per iteration) verifies the effectiveness of the HTE integration. In terms of accuracy, the method maintains stability, with the KL relative error remaining in the order of 10^{-3} and negligible fluctuations in log-domain errors. The model complexity grows linearly with dimension (from 76k to 117k parameters), indicating that A-PFRM provides a scalable solution for high-dimensional problems.

5.4. High-dimensional test problems with non-Gaussian solutions. In this subsection, we consider the time-decaying Geometric Ornstein-Uhlenbeck (GOU) process, whose distribution no longer possesses Gaussian characteristics such as rapid decay, symmetry, and full domain. The features of its heavy tail and positive semi-axis support pose significant challenges to the numerical stability and boundary handling capability.

This problem is defined on the positive orthant $X_t \in \mathbb{R}_+^d$ and involves a heavy-tailed Log-Normal distribution. The SDE is given by:

$$(5.46) \quad dX_t = e^{-t} \left[\theta(c - \log X_t) + \frac{1}{2} \sigma \odot \sigma \right] \odot X_t dt + e^{-\frac{t}{2}} \text{diag}(X_t \odot \sigma) dW_t,$$

$$(5.47) \quad X_0 \sim p_0 = \log \mathcal{N}(\mu_0, \Sigma_0), \quad t \in [0, 1],$$

where \odot denotes the Hadamard product, $\theta = 1.0$ controls the reversion speed. To ensure the generality of the high-dimensional benchmark, the long-term mean parameter $c \in \mathbb{R}^d$ and the volatility vector $\sigma \in \mathbb{R}^d$ are randomly initialized. Specifically, each element is sampled from uniform distributions: $c_i \sim \text{Uniform}([0.7, 1.3])$ and $\sigma_i \sim \text{Uniform}([0.3, 0.7])$. The drift term is now both state- and time-dependent:

$$(5.48) \quad f(x, t) = e^{-t} \left(\theta(c - \log x) + \frac{1}{2} \sigma \odot \sigma \right) \odot x.$$

The diffusion term is $G(x, t) = e^{-\frac{t}{2}} \text{diag}(x \odot \sigma)$, resulting in the time-varying diffusion matrix:

$$(5.49) \quad D(x, t) = \frac{1}{2} G(x, t) G(x, t)^T = \frac{1}{2} e^{-t} \text{diag}(x \odot x \odot \sigma \odot \sigma).$$

The FP equation governs the evolution of the Log-Normal density on \mathbb{R}_+^d :

$$(5.50) \quad \frac{\partial p_t(\mathbf{x})}{\partial t} = -\nabla \cdot [\mathbf{f}(\mathbf{x}, t)p_t(\mathbf{x})] + \sum_{i,j=1}^d \frac{\partial^2}{\partial x_i \partial x_j} [D_{ij}(\mathbf{x}, t)p_t(\mathbf{x})],$$

$$(5.51) \quad \int_{\mathbb{R}_+^d} p_t(\mathbf{x}) = 1, \quad p_t(\mathbf{x}) \geq 0, \quad \forall t \in [0, 2],$$

$$(5.52) \quad p_0(\mathbf{x}) = \log \mathcal{N}(\boldsymbol{\mu}_0, \boldsymbol{\Sigma}_0),$$

where $\boldsymbol{\mu}_0 = \mathbf{1}$ and $\boldsymbol{\Sigma}_0$ is constructed to be symmetric and strictly positive definite to ensure a well-conditioned initial distribution. We generate a random auxiliary matrix $\mathbf{Q} \in \mathbb{R}^{d \times d}$ with entries drawn from a standard normal distribution $\mathcal{N}(0, 1)$, and construct $\boldsymbol{\Sigma}_0$ as:

$$(5.53) \quad \boldsymbol{\Sigma}_0 = \frac{0.5}{\|\mathbf{Q}\mathbf{Q}^T\|_F} \mathbf{Q}\mathbf{Q}^T + 0.1\mathbf{I}_d,$$

where $\|\cdot\|_F$ denotes the Frobenius norm and \mathbf{I}_d is the identity matrix. The term $0.1\mathbf{I}_d$ acts as a regularization to guarantee the minimal eigenvalue is bounded away from zero, preventing numerical singularity in high dimensions. Despite the complexity, the exact solution can be derived analytically by introducing a time-rescaling variable $\tau(t) = \int_0^t e^{-s} ds = 1 - e^{-t}$. The solution $p_t(\mathbf{x})$ is an anisotropic Log-Normal distribution $\log \mathcal{N}(\boldsymbol{\mu}_t, \boldsymbol{\Sigma}_t)$ with parameters evolving as:

$$(5.54) \quad \boldsymbol{\mu}_t = \mathbf{c} + e^{-\theta\tau(t)}(\boldsymbol{\mu}_0 - \mathbf{c}),$$

$$(5.55) \quad \boldsymbol{\Sigma}_t = \boldsymbol{\Sigma}_\infty - e^{-2\theta\tau(t)}(\boldsymbol{\Sigma}_\infty - \boldsymbol{\Sigma}_0),$$

where the stationary covariance $\boldsymbol{\Sigma}_\infty$ satisfies $2\theta\boldsymbol{\Sigma}_\infty = \text{diag}(\boldsymbol{\sigma} \odot \boldsymbol{\sigma})$.

The velocity field for this time-decaying GOU problem is:

$$(5.56) \quad \mathbf{v}_t(\mathbf{x}) = \mathbf{f}(\mathbf{x}, t) - \nabla \cdot \mathbf{D}(\mathbf{x}, t) - \mathbf{D}(\mathbf{x}, t)\nabla \log p_t(\mathbf{x}).$$

hence the loss function is formulated as:

$$(5.57) \quad \mathcal{L}(\theta) = \mathbb{E}_{(\mathbf{x}, t) \sim \mathcal{D}} \left[\|\mathbf{u}_\theta(\mathbf{x}, t) - \mathbf{f}(\mathbf{x}, t) + \nabla \cdot \mathbf{D}(\mathbf{x}, t) + \mathbf{D}(\mathbf{x}, t)\nabla \log \hat{p}_t(\mathbf{x}; \theta)\|_2^2 \right].$$

where the initial sampling distribution is $\mathcal{D}_0 = \text{Uniform}(\Omega \times [0, 1])$: domain of interest is $\Omega = [1 \times 10^{-6}, 14]^d$ (avoiding the singularity at 0) with sample batch size $N_x = 1024$ and the time schedule is $\{0.05 \cdot s\}_{s=1}^{20} \subset (0, 1]$.

For test problems with $d = 4, 8, 12$, we generate the initial parameters Θ_0 with Kaiming initialization and construct a neural network which contains 2 fully connected hidden layers with 256 neurons. The solver of the CNF-augmented ODE system is set to the RK-4 method with a step size of 0.05. The total number of training epochs is set to $N_{\text{epoch}} = 500$ with warm-up epochs $N_{\text{warmup}} = 150$ and ramp-up epochs $N_{\text{rampup}} = 150$. The final adaptive sampling ratio is set to $\alpha_{\text{adapt}} = 0.8$. The learning rate for Adam optimizer is set to $\eta = 0.0001$. Here, we select a set of testing time snapshots $t_{\text{test}} = \{0.1, 0.25, 0.5, 0.75, 1.0\}$ for validation.

Table 5.6 presents the comparative results for $d = 4, 8, 12$ GOU process, which features heavy-tailed Log-Normal distributions. The baseline tKRnet shows a degradation in approximation fidelity in this non-Gaussian regime, yielding relative errors in the log-domain (L_2 and L_∞) exceeding 5.0 across all tested dimensions. This suggests difficulties in capturing the heavy-tailed structure and the scale of the density. Conversely, A-PFRM maintains stable L_2 relative errors (approximately 0.3) and achieves KL relative errors in the order of 10^{-4} ,

TABLE 5.6
Results for 4D, 8D, and 12D test problems with non-Gaussian solutions.

Dimension	4D		8D		12D	
	tKRnet	A-PFRM	tKRnet	A-PFRM	tKRnet	A-PFRM
KL Rel. Err.	8.200E-3	6.037E-4	1.047E-2	7.725E-4	–	1.165E-3
LL L_2 Rel. Err.	8.541E+0	3.429E-1	6.682E+0	2.980E-1	–	2.491E-1
LL L_∞ Rel. Err.	5.407E+0	9.025E-1	6.315E+0	9.021E-1	–	8.937E-1
Total Epochs	6×200	500	6×200	500	6×200	500
Time per Epoch (s)	16.02	10.33	69.26	13.12	165.17	16.52
Total Time (s)	19,224	5,165	83,112	6,560	–	8,260
# Parameters	385,531	68,356	913,597	70,408	1,457,743	72,460

* tKRnet results are reported using $k = 6$ iterations.

– Indicates training was not completed due to excessive computational cost.

which are over one order of magnitude lower than the baseline. Computationally, A-PFRM overcomes the bottleneck observed in the baseline at 12D (where tKRnet requires 165 s per epoch), completing the training in 2.3 hours using a model that is 20 times more compact (72k vs. 1.46M parameters).

For test problems with $d = 20, 40, 60, 100$, we expand the scale of the neural network, which contains 2 fully connected hidden layers with 512 neurons. The network initialization and ODE solver are consistent with the setting in the $d = 4, 8, 12$ test problems. Here, we also employ the HTE to accelerate the computation of divergence in CNF augmented ODE. The total number of training epochs is set to $N_{\text{epoch}} = 800$ with warm-up epochs $N_{\text{warmup}} = 200$ and ramp-up epochs $N_{\text{rampup}} = 200$. The final adaptive sampling ratio is set to $\alpha_{\text{adapt}} = 0.8$. The learning rate for Adam optimizer is set to $\eta = 0.0001$. The test time snapshots $t_{\text{test}} = \{0.1, 0.25, 0.5, 0.75, 1.0\}$ remain the same.

TABLE 5.7
Results for 20D, 40D, 60D and 100D test problems with non-Gaussian solutions.

Dimension	20D	40D	60D	100D
	A-PFRM with HTE			
KL Rel. Err.	2.701E-4	7.537E-4	1.206E-3	2.518E-3
LL L_2 Rel. Err.	2.078E-1	1.724E-1	1.630E-1	1.415E-1
LL L_∞ Rel. Err.	8.324E-1	7.534E-1	7.111E-1	6.551E-1
Total Epochs	800	800	800	800
Time per Epoch (s)	6.58	6.51	6.49	6.53
Total Time (s)	5,264	5,208	5,192	5,224
# Parameters	284,180	304,680	325,180	366,180

Table 5.7 presents the results for higher dimensions GOU problems using A-PFRM with HTE. Consistent with the Gaussian benchmark, the training time remains virtually invariant to dimensionality, fluctuating around 6.5 seconds per epoch as the dimension increases from 20D to 100D. The method demonstrates robustness in modeling heavy-tailed anisotropic distributions in high-dimensional spaces, with the KL relative error stabilizing at the order of 10^{-3} . The model complexity exhibits linear growth, further validating A-PFRM as a lightweight and precise solver for high-dimensional stochastic systems with non-Gaussian

solutions.

6. Conclusion. In this work, we have presented the Adaptive Probability Flow Residual Minimization (A-PFRM), a novel deep learning framework that effectively mitigates the CoD in solving high-dimensional FP equations. By reformulating the second-order FP equation into an equivalent deterministic PF-ODE, we transform the optimization landscape from minimizing a Hessian-dependent PDE residual to minimizing a Jacobian-dependent ODE residual. This order reduction strategy fundamentally circumvents the computational bottleneck that has long constrained standard physics-informed approaches, offering a scalable pathway for high-dimensional scientific computing.

The efficacy of the proposed framework is characterized by its scalability, theoretical rigor, and robustness. By integrating CNFs with the HTE, A-PFRM decouples the computational cost from dimensionality, achieving effectively $O(1)$ wall-clock training time on parallel GPU architectures. This allows the method to scale efficiently to 100 dimensions with constant temporal overhead. Theoretically, we provide a theoretical analysis linking the sampling strategy to error bounds, proving that generative adaptive sampling is not merely a heuristic strategy but a necessary condition to minimize the $\hat{\rho}_t$ -weighted residual norm required to bound the Wasserstein distance. Numerical experiments further validate these properties, demonstrating that A-PFRM retains high accuracy even in challenging regimes where baselines encounter difficulties, particularly for systems with time-varying diffusion tensors and non-Gaussian, heavy-tailed distributions.

Beyond the specific context of FP equations, the first-order residual paradigm suggests a generalizable roadmap: leveraging the equivalence between macroscopic PDEs and microscopic probability flows to reduce differential orders, thereby rendering complex physical systems tractable for neural solvers. Future work will explore extending this framework to bounded domains with complex boundary conditions, as well as applying this velocity-centric perspective to high-dimensional optimal control and inverse problems.

REFERENCES

- [1] I. BABUŠKA, F. NOBILE, AND R. TEMPONE, *A stochastic collocation method for elliptic partial differential equations with random input data*, SIAM Journal on Numerical Analysis, 45 (2007), pp. 1005–1034.
- [2] A. G. BAYDIN, B. A. PEARLMUTTER, A. A. RADUL, AND J. M. SISKIND, *Automatic differentiation in machine learning: a survey*, Journal of Machine Learning Research, 18 (2018), pp. 1–43.
- [3] N. M. BOFFI AND E. VANDEN-EIJNDEN, *Probability flow solution of the Fokker-Planck equation*, Machine Learning: Science and Technology, 4 (2023), p. 035012.
- [4] C. BRENNAN AND D. VENTURI, *Data-driven closures for stochastic dynamical systems*, Journal of Computational Physics, 372 (2018), pp. 281–298.
- [5] R. E. CAFLISCH, *Monte Carlo and quasi-Monte Carlo methods*, Acta Numerica, 7 (1998), pp. 1–49.
- [6] Z. CAI, Y. CAO, Y. HUANG, AND X. ZHOU, *Weak generative sampler to efficiently sample invariant distribution of stochastic differential equation*, arXiv preprint arXiv:2405.19256, (2024).
- [7] R. T. Q. CHEN, Y. RUBANOVA, J. BETTENCOURT, AND D. K. DUVENAUD, *Neural ordinary differential equations*, in Advances in Neural Information Processing Systems, vol. 31, 2018.
- [8] X. CHEN, L. YANG, J. DUAN, AND G. E. KARNIADAKIS, *Solving inverse stochastic problems from discrete particle observations using the Fokker-Planck equation and physics-informed neural networks*, SIAM Journal on Scientific Computing, 43 (2021), pp. B811–B830.
- [9] H. CHO, D. VENTURI, AND G. E. KARNIADAKIS, *Numerical methods for high-dimensional probability density function equations*, Journal of Computational Physics, 305 (2016), pp. 817–837.
- [10] G. CYBENKO, *Approximation by superpositions of a sigmoidal function*, Mathematics of Control, Signals and Systems, 2 (1989), pp. 303–314.
- [11] L. DINH, D. KRUEGER, AND Y. BENGIO, *NICE: Non-linear independent components estimation*, in International Conference on Learning Representations, 2015.
- [12] W. E AND B. YU, *The deep Ritz method: a deep learning-based numerical algorithm for solving variational problems*, Communications in Mathematics and Statistics, 6 (2018), pp. 1–12.

- [13] H. C. ELMAN, D. J. SILVESTER, AND A. J. WATHEN, *Finite elements and fast iterative solvers: with applications in incompressible fluid dynamics*, Oxford University Press, 2014.
- [14] L. C. EVANS, *Partial differential equations*, vol. 19 of Graduate Studies in Mathematics, American Mathematical Society, 2022.
- [15] X. FENG, L. ZENG, AND T. ZHOU, *Solving time dependent Fokker-Planck equations via temporal normalizing flow*, *Communications in Computational Physics*, 32 (2022), pp. 401–423.
- [16] J. FOO, X. WAN, AND G. E. KARNIADAKIS, *The multi-element probabilistic collocation method (ME-PCM): Error analysis and applications*, *Journal of Computational Physics*, 227 (2008), pp. 9572–9595.
- [17] Z. GAO, L. YAN, AND T. ZHOU, *Failure-informed adaptive sampling for PINNs*, *SIAM Journal on Scientific Computing*, 45 (2023), pp. A1971–A1994.
- [18] D. T. GILLESPIE, *Exact stochastic simulation of coupled chemical reactions*, *The Journal of Physical Chemistry*, 81 (1977), pp. 2340–2361.
- [19] I. GOODFELLOW, J. POUGET-ABADIE, M. MIRZA, B. XU, D. WARDE-FARLEY, S. OZAIR, A. COURVILLE, AND Y. BENGIO, *Generative adversarial nets*, in *Advances in Neural Information Processing Systems*, vol. 27, 2014, pp. 2672–2680.
- [20] W. GRATHWOHL, R. T. Q. CHEN, J. BETTENCOURT, I. SUTSKEVER, AND D. DUVENAUD, *FFJORD: Free-form continuous dynamics for scalable reversible generative models*, in *International Conference on Learning Representations*, 2019.
- [21] J. HE, Q. LIAO, AND X. WAN, *Adaptive deep density approximation for stochastic dynamical systems*, *Journal of Scientific Computing*, 102 (2025), p. 57.
- [22] K. HE, X. ZHANG, S. REN, AND J. SUN, *Delving deep into rectifiers: Surpassing human-level performance on imagenet classification*, in *Proceedings of the IEEE International Conference on Computer Vision*, 2015, pp. 1026–1034.
- [23] D. J. HIGHAM, *An algorithmic introduction to numerical simulation of stochastic differential equations*, *SIAM Review*, 43 (2001), pp. 525–546.
- [24] Z. HU, Z. ZHANG, G. E. KARNIADAKIS, AND K. KAWAGUCHI, *Score-based physics-informed neural networks for high-dimensional Fokker-Planck equations*, *SIAM Journal on Scientific Computing*, 47 (2025), pp. C680–C705.
- [25] Z. JIN, W. ZAN, S. MA, AND W. JIA, *Physics-informed neural networks with hybrid sampling for stationary Fokker-Planck-Kolmogorov equation*, *Physica A: Statistical Mechanics and its Applications*, 663 (2025), p. 130434.
- [26] D. P. KINGMA AND J. BA, *Adam: A method for stochastic optimization*, in *International Conference on Learning Representations*, 2015.
- [27] I. KOBYZEV, S. J. PRINCE, AND M. A. BRUBAKER, *Normalizing flows: An introduction and review of current methods*, *IEEE Transactions on Pattern Analysis and Machine Intelligence*, 43 (2020), pp. 3964–3979.
- [28] H. LEI, X. YANG, B. ZHENG, G. LIN, AND N. A. BAKER, *Constructing surrogate models of complex systems with enhanced sparsity: quantifying the influence of conformational uncertainty in biomolecular solvation*, *Multiscale Modeling & Simulation*, 13 (2015), pp. 1327–1353.
- [29] M. LESHNO, V. Y. LIN, A. PINKUS, AND S. SCHOCKEN, *Multilayer feedforward networks with a nonpolynomial activation function can approximate any function*, *Neural Networks*, 6 (1993), pp. 861–867.
- [30] L. LI, S. HURAUULT, AND J. M. SOLOMON, *Self-consistent velocity matching of probability flows*, in *Advances in Neural Information Processing Systems*, vol. 36, 2023, pp. 57038–57057.
- [31] Y. LIPMAN, R. T. CHEN, H. BEN-HAMU, M. NICKEL, AND M. LE, *Flow matching for generative modeling*, in *International Conference on Learning Representations*, 2023.
- [32] G. J. LORD, C. E. POWELL, AND T. SHARDLOW, *An introduction to computational stochastic PDEs*, vol. 50, Cambridge University Press, 2014.
- [33] X. MA AND N. ZABARAS, *An adaptive hierarchical sparse grid collocation algorithm for the solution of stochastic differential equations*, *Journal of Computational Physics*, 228 (2009), pp. 3084–3113.
- [34] A. NARAYAN AND D. XIU, *Stochastic collocation methods on unstructured grids in high dimensions via interpolation*, *SIAM Journal on Scientific Computing*, 34 (2012), pp. A1729–A1752.
- [35] B. ØKSENDAL, *Stochastic Differential Equations: An Introduction with Applications*, Universitext, Springer Berlin Heidelberg, 2010.
- [36] G. PAPAMAKARIOS, E. NALISNICK, D. J. REZENDE, S. MOHAMED, AND B. LAKSHMINARAYANAN, *Normalizing flows for probabilistic modeling and inference*, *Journal of Machine Learning Research*, 22 (2021), pp. 1–64.
- [37] A. PASZKE, S. GROSS, F. MASSA, ET AL., *PyTorch: An imperative style, high-performance deep learning library*, in *Advances in Neural Information Processing Systems*, vol. 32, 2019, pp. 8024–8035.
- [38] M. RAISSI, P. PERDIKARIS, AND G. E. KARNIADAKIS, *Physics-informed neural networks: A deep learning framework for solving forward and inverse problems involving nonlinear partial differential equations*, *Journal of Computational Physics*, 378 (2019), pp. 686–707.
- [39] D. REZENDE AND S. MOHAMED, *Variational inference with normalizing flows*, in *International Conference on Machine Learning*, 2015, pp. 1530–1538.
- [40] H. RISKEN, *Fokker-Planck equation*, in *The Fokker-Planck Equation: Methods of Solution and Applications*,

- Springer, 1989, pp. 63–95.
- [41] D. W. SCOTT, *Multivariate density estimation: theory, practice, and visualization*, John Wiley & Sons, 2015.
 - [42] B. SEPEHRIAN AND M. K. RADPOOR, *Numerical solution of non-linear Fokker-Planck equation using finite differences method and the cubic spline functions*, *Applied Mathematics and Computation*, 262 (2015), pp. 187–190.
 - [43] J. SIRIGNANO AND K. SPILIOPOULOS, *DGM: A deep learning algorithm for solving partial differential equations*, *Journal of Computational Physics*, 375 (2018), pp. 1339–1364.
 - [44] K. SOBCZYK, *Stochastic differential equations: with applications to physics and engineering*, vol. 40, Springer Science & Business Media, 2013.
 - [45] Y. SONG, J. SOHL-DICKSTEIN, D. P. KINGMA, A. KUMAR, S. ERMON, AND B. POOLE, *Score-based generative modeling through stochastic differential equations*, in *International Conference on Learning Representations*, 2021.
 - [46] K. TANG, X. WAN, AND Q. LIAO, *Deep density estimation via invertible block-triangular mapping*, *Theoretical and Applied Mechanics Letters*, 10 (2020), pp. 143–148.
 - [47] K. TANG, X. WAN, AND Q. LIAO, *Adaptive deep density approximation for Fokker-Planck equations*, *Journal of Computational Physics*, 457 (2022), p. 111080.
 - [48] K. TANG, X. WAN, AND C. YANG, *DAS-PINNs: A deep adaptive sampling method for solving high-dimensional partial differential equations*, *Journal of Computational Physics*, 476 (2023), p. 111868.
 - [49] X. TANG AND L. YING, *Solving high-dimensional Fokker-Planck equation with functional hierarchical tensor*, *Journal of Computational Physics*, 511 (2024), p. 113110.
 - [50] C. VILLANI, *Optimal Transport: Old and New*, vol. 338 of *Grundlehren der mathematischen Wissenschaften*, Springer Berlin Heidelberg, 2009.
 - [51] D. XIU, *Numerical methods for stochastic computations: a spectral method approach*, Princeton University Press, 2010.
 - [52] D. XIU AND J. S. HESTHAVEN, *High-order collocation methods for differential equations with random inputs*, *SIAM Journal on Scientific Computing*, 27 (2005), pp. 1118–1139.
 - [53] J. ZHAI, M. DOBSON, AND Y. LI, *A deep learning method for solving Fokker-Planck equations*, in *Mathematical and Scientific Machine Learning*, PMLR, 2022, pp. 568–597.
 - [54] J. ZHAO, M. ZHOU, X. ZUO, AND W. LI, *Variational conditional normalizing flows for computing second-order mean field control problems*, arXiv preprint arXiv:2503.19580, (2025).